

CHAPTER IV

COLLISION-INDUCED ROTATIONAL ALIGNMENT OF N_2^+ DRIFTED IN He

A. Introduction

Collision-induced rotational alignment can be produced whenever there exist anisotropies both in the interaction potential and relative velocity vector distribution of the colliding partners. The phenomenon has been observed often in supersonic jet expansions, in which the latter anisotropy is created by the velocity slip of the seed and carrier in the expansion. For example, substantial degrees of alignment are reported for sodium dimer expanded in sodium,¹ for I_2 seeded in Ar, He, and H_2 ,^{2,3} and for the expansion of CO_2 seeded in Ar, He, and H_2 .⁴ All of the aforementioned studies incorporate some form of optical detection of the alignment, either laser-induced fluorescence or infrared absorption. Additionally, all of these studies find a general propensity for the rotational angular momentum vectors to be aligned perpendicular to the jet expansion direction.

However, only a few studies to date have incorporated some distinct form of selection of the velocity component *along* the jet expansion axis. The most notable is the work of Aquilanti and colleagues in experiments performed on a supersonic jet expansion coupled to a molecular beam velocity-selector and Stern-Gerlach apparatus. A dramatic correlation between velocity subgroup and alignment has been demonstrated on both neutral O_2 ^{5,6} and neutral N_2 ⁷ expanded in various carrier gases.

In the most extreme case of O_2 expanded in He, the polarization varied from essentially zero in the low-velocity tail of the beam to greater than 80% in the high-velocity tail. More recently, Wodtke and colleagues, using the technique of quantum-state specific metastable time-of-flight spectroscopy, studied two rotational states, $J = 4$ and 6 , of CO expanded in He, and found velocity alignment correlations that, *prima facie*, appear to contradict the work of Aquilanti.^{8,9} Unfortunately, both of these investigators cite the work presented here to buttress their arguments, placing this investigator in a decidedly uncomfortable position. Additionally, all of these observations have been on neutral-neutral systems.

The external electric field of a drift tube also creates an anisotropic distribution of relative velocities and thus, the possibility of alignment. The first observation of collision-induced rotational alignment in an ion-neutral system was reported by Dressler *et al.*¹⁰ in a much earlier incarnation of the drift-tube apparatus used in the present work. The $N_2^+(v'' = 0)$ ions drifted in He were studied by polarized LIF with a broadband Nd:YAG pumped dye laser. By probing perpendicular to the tube axis at 14 Td (corresponding to an average center-of-mass collision energy of 52 meV), Dressler *et al.* measured fully velocity-averaged polarization coefficients for two rotational states, $N''=4$ and $N''=10$. They found a corresponding $A_0^{(2)}$ quadrupole alignment parameter of -0.11 ± 0.05 for both states, the sign and magnitude indicating a significant preference for the rotational angular momentum vectors to be aligned perpendicular to the drift field, as discussed further in Sec. IV.B below.

This early drift-tube study subsequently motivated theoretical work by Follmeg, Rosmus, Werner, and colleagues. In a series of three papers, a ground-state *ab initio* N_2^+ -He interaction potential was calculated¹¹ (as discussed in Sec. I.B), and both quantum close-coupled (CC)¹² and classical-trajectory¹³ scattering calculations were performed with this potential surface, using as a framework a steady-state kinetics or master equation formalism and semi-empirical relative velocity vector distribution previously developed by Meyer and Leone.¹⁴ This theoretical work produced qualitative but not quantitative agreement with the experimentally-determined alignment parameters. Specifically, the theoretical CC $A_0^{(2)}$ values were found to be -0.010 and -0.034 for the $N'' = 4$ and 10 states, respectively, smaller in absolute value than the experimental parameters by factors of 11 and 3. A better agreement could be reached by adjusting the second coefficient of the Legendre moment expansion of the relative velocity vector distribution, underscoring the importance of the precise degree of anisotropy in the distribution of relative velocity vectors as well as in the interaction potential for determining the resultant steady-state alignment. The steady-state fully-velocity averaged theory is summarized in Sec. IV.F below, and the reasons why this theory is not appropriate for the current experiment are discussed.

Unfortunately, this first N_2^+ -He experiment had several shortcomings. In particular, the low duty cycle of the pulsed laser resulted in inherently poor signal-to-background; to obtain adequate signal, the dye laser had to be run with sufficient power to saturate the transitions, introducing further complications to the data

analysis.¹⁵ Additionally, the broad linewidth of the laser (approximately 0.9 cm^{-1}) meant that the first experiment was incapable of resolving velocity-subgroup alignment, or any details about the underlying velocity component distributions. The current single-frequency version of the experiment circumvents both of these shortcomings and represents the “state of the art” of drift-tube alignment experiments. Because, to the best of this investigator’s knowledge, only one other JILA thesis¹⁶ has investigated collision-induced rotational alignment, a more extensive treatment of background material is presented in Secs. IV.B and C. Section IV.D discusses results of two different types of alignment experiments, and Sec. IV.E covers diagnostic experiments conducted. A discussion of the underlying dynamics is given in Sec. IV.F. Section IV.G wraps up with an conclusion.

B. Descriptive theory

The brief overview of the descriptive theory of the detection of rotational alignment is given in this section. Section IV.B.1 covers the phenomenon at an elementary level, with simple qualitative descriptions and observations. Section IV.B.2 treats classical rigid-rotor theory, while Sec. IV.B.3 outlines the quantum theory. Section IV.B.4 discusses extensions and approximations to the quantum theory that are particularly relevant for this work.

1. Qualitative & heuristic arguments

A cartoon diagram of the basic geometry of the canonical LIF probe-measurement scheme used in this work is shown in Fig. 4.1. The drift field is along the laboratory Z-axis, and the fluorescence detector is placed along the Y-axis. The two laser probe directions employed are shown: the coaxial probe direction along the

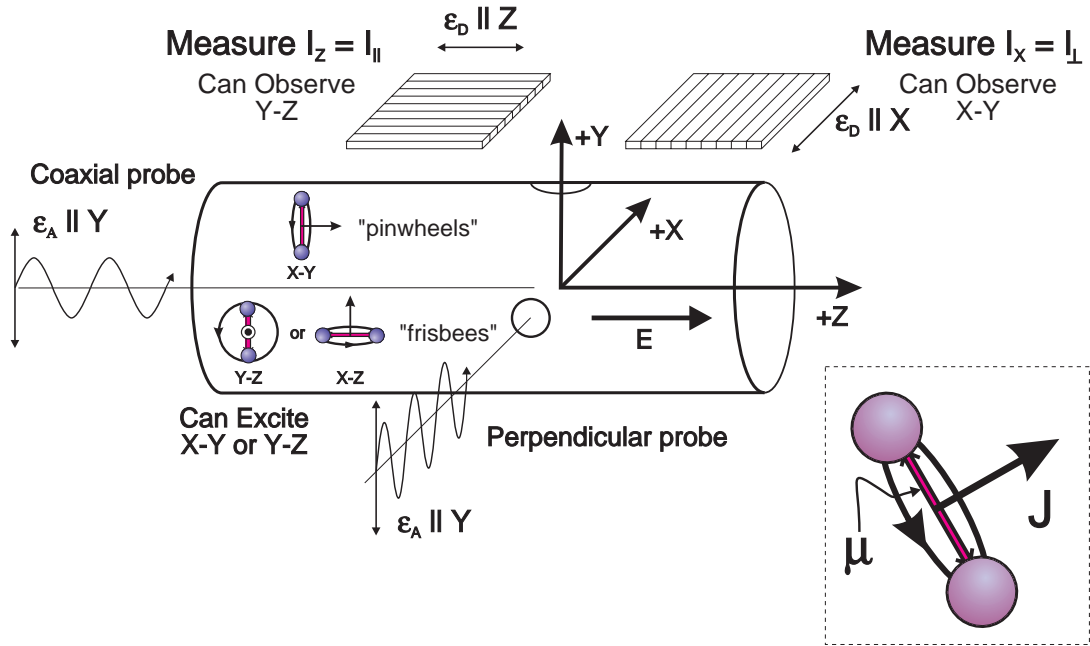


Fig. 4.1: Cartoon diagram of LIF probe-detection scheme.

field or symmetry axis ($\hat{k}_{laser} \parallel Z$) and the perpendicular probe direction ($\hat{k}_{laser} \parallel X$). The laser polarization vector $\hat{\epsilon}_A$ for either of these probe directions is fixed parallel to the detection axis.

Classically, a diatomic molecule can be modeled as a rigid rotor with its rotational angular momentum \mathbf{J} always fixed perpendicular to the internuclear axis, as shown in the inset of Fig. 4.1. The rotor axis has three mutually orthogonal planes of rotation in the lab frame: the X-Y, Y-Z, and X-Z planes. Because of the cylindrical symmetry of the drift tube, the latter two planes are physically equivalent. Hence, there are two distinct senses of molecular rotation: the X-Y plane of rotation with $\mathbf{J} \parallel Z_{lab}$, referred to here as “pinwheels”, and the Y-Z plane with $\mathbf{J} \perp Z_{lab}$, referred to as “frisbees”. The essence of any collision-induced alignment experiment is to formulate a scheme of distinguishing between these two types of rotation. In a LIF experiment, this information is obtained by knowing how the absorption and emission dipole moments are tied to the molecular framework, i.e., how the molecule is “built”. For the particular system studied here, we are concerned with $\Sigma - \Sigma$ or parallel transitions, which means the induced electric dipole moment $\hat{\mu}$ lies along the internuclear axis, in the plane of rotation of the molecule.

For the probe scheme shown in Fig. 4.1, the laser picks out both the X-Y and Y-Z planes of rotation with dot-product efficiency $\hat{\mu} \cdot \hat{\epsilon}_A$. The fluorescence polarizer then distinguishes between these two senses by selectively attenuating either the pinwheel (X-Y) or frisbee (Y-Z) emission with dot-product efficiency $\hat{\mu} \cdot \hat{\epsilon}_D$. Placing the polarizer so that its transmission axis $\hat{\epsilon}_D$ is along Z preferentially selects the

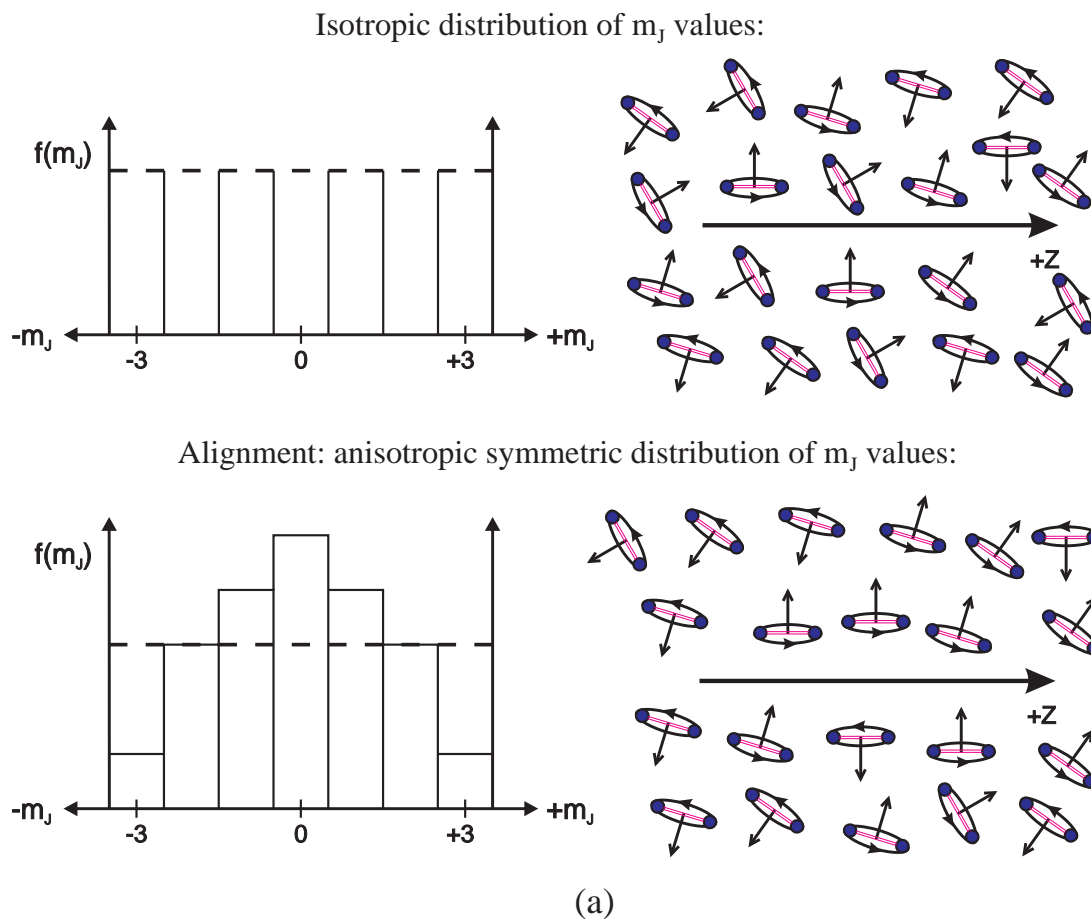
frisbee fluorescence, of intensity I_Z or I_{\parallel} ; rotating the polarizer 90 degrees so that $\hat{\epsilon}_D$ is along X selects the pinwheel fluorescence, of intensity I_X or I_{\perp} . Then the basic experimental parameter for probing with vertically polarized light is the linear polarization coefficient

$$P = \frac{I_{\parallel} - I_{\perp}}{I_{\parallel} + I_{\perp}} \quad (4.1)$$

reported in this work as a percentage ($P \times 100\%$).

A very simple physical picture of collision-induced rotational alignment is given by the model first suggested by Gorter,¹⁷ who pointed out that the hard-ellipsoidal collisional cross section of a rotating molecule is orientation dependent and, for linear molecules, is minimized when the angular momentum vectors \mathbf{J} are aligned perpendicular to the flow direction. Thus, one would expect to observe a propensity for more frisbee-like than pinwheel-like molecules in a drift tube experiment. Since frisbees are associated with fluorescence intensity I_{\parallel} and pinwheels associated with intensity I_{\perp} , this simple model would in general predict positive polarization coefficients to be observed in any collision-induced alignment experiment.

Figures 4.2 (a) and (b) are cartoons of the corresponding m_J distribution picture for the simple rigid-rotor model. In the isotropic case (no alignment), all projections of \mathbf{J} onto Z_{lab} are equally likely. For the expected case of preferential population of frisbee-like planes of rotation, the polarization coefficients are positive, $m_J = 0$ is more likely than $m_J = J$, and the m_J distribution is bowed down. The



$$P(\chi_A = 90^\circ) = \frac{I_{\parallel} - I_{\perp}}{I_{\parallel} + I_{\perp}}$$

To first approximation, can think of sign of $P(90^\circ)$ as determining overall "bow" of m_j distribution and quadrupole alignment parameter $A_0^{(2)}$

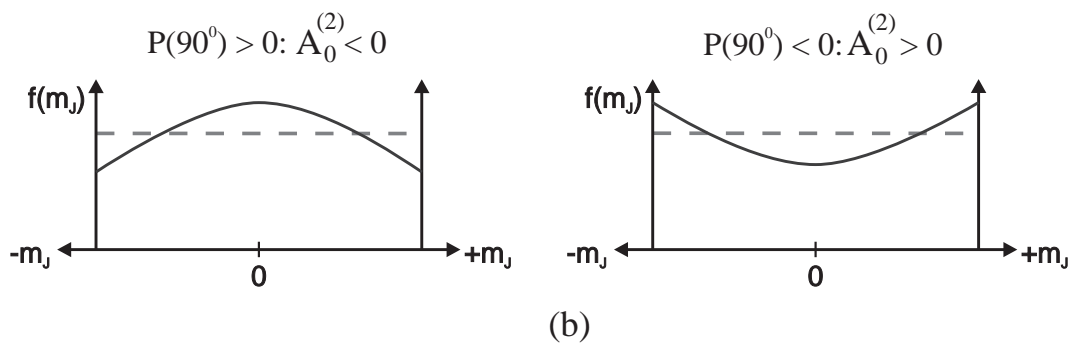


Fig 4.2: Cartoon m_j distribution picture. (a) isotropic and aligned distributions for $J = 3$ case (b) qualitative meaning of polarization coefficients and alignment parameters in terms of "bow" of m_j distributions.

converse holds for preferential population of the pinwheel-like plane of rotation: the polarization coefficients are negative and the m_J distribution is bowed up. In the dominant moment approximation discussed below in Sec. IV.B.4, only the leading nonisotropic term, the quadrupole alignment parameter $A_0^{(2)}$, is retained. With this approximation, and the measurement scheme just outlined, the linear polarization coefficients have a very simple interpretation, as illustrated in Fig. 4.2 (b). A polarization coefficient of zero indicates no rotational alignment, while positive (negative) polarization coefficients are associated with negative (positive) quadrupole alignment parameters, which in turn indicate a preference for population of the frisbee (pinwheel) planes of rotation.

One of the primary advantages of the geometry of the above scheme is that in principle, the measurements should be free of isotropic polarization, which in general can be defined as the presence of a predictably nonzero polarization signal even in the complete absence of molecular alignment. Isotropic polarization is discussed more quantitatively in the following sections; however there is a simple symmetry heuristic argument that can be used to predict whether or not a measurement scheme will exhibit isotropic polarization. As can be seen from Fig. 4.1, the vector $\hat{\epsilon}_D$ always remains perpendicular to $\hat{\epsilon}_A$ for either the I_{\parallel} or I_{\perp} measurement. As discussed below, isotropic polarization will always be modulated as $P_2(\cos\chi_{AD})$, where χ_{AD} is the angle between $\hat{\epsilon}_A$ and $\hat{\epsilon}_D$. For the chosen geometry, however, this angle is fixed to 90 degrees no matter how $\hat{\epsilon}_D$ is rotated, which suggests that no modulation in fluorescence intensity should be observed as $\hat{\epsilon}_D$ is rotated. If a different measurement

scheme had been chosen—for example, one in which horizontally polarized light was used, then the angle χ_{AD} will change depending on how $\hat{\epsilon}_D$ is rotated, and the fluorescence signal will modulate. Loosely, this is because there is a geometric coincidence between the $\hat{\epsilon}_A$ and $\hat{\epsilon}_D$ vectors that permits efficient detection of the dipole emission.

2. *Simple classical theory*

The simple classical rigid rotor model of the previous section is extended to produce a J-independent LIF intensity expression for the two laser probe directions, as a function of the orientation of the two polarization vectors $\hat{\epsilon}_A$ and $\hat{\epsilon}_D$. The treatment here is quite similar to models previously developed by Sinha *et al.*¹ and Sanders *et al.*,¹⁸ but explicitly addresses the coaxial probe geometry. Additionally, resulting expressions are found which correspond to the quantum treatment outlined below in Sect. IV.B.3 in the high-J limit. High-J limit expressions are frequently used in the analysis of experiments where large angular momentum quantum numbers are encountered. This treatment is particularly convenient because no angular momentum recoupling terms need be calculated.

In this model, the transition moment $\hat{\mu}$ is treated as a classical electric dipole, tied to the geometry of the molecule. Only $\Sigma - \Sigma$ (parallel) transitions, with $\hat{\mu}$ lying along the internuclear axis are considered here. The absorption and emission dot products $\hat{\mu} \cdot \hat{\epsilon}_A$ and $\hat{\mu} \cdot \hat{\epsilon}_D$ still contain the essential geometrical information about the alignment of the molecules. But now, the resulting LIF intensity is treated as a

function of the two angles that can be conveniently controlled in a polarized LIF experiment, χ_A and χ_D , as illustrated in Fig. 4.3.

The fluorescence intensity expression as a function of (χ_A, χ_D) is produced by averaging over the distribution of angular momentum vectors according to

$$I_{LIF}(\chi_A, \chi_D; \hat{k}_{laser}) = K \int_0^{2\pi} d\varphi \int_0^\pi d\theta \sin\theta n(\theta) \langle (\hat{\epsilon}_A \cdot \hat{\mu}_{lab})^2 \rangle \langle (\hat{\epsilon}_D \cdot \hat{\mu}_{lab})^2 \rangle \quad (4.2)$$

where K is an arbitrary rescaling constant, (θ, φ) are the polar angles of \mathbf{J} with respect to Z_{lab} , and $\hat{\mu}_{lab}$ is the transition moment of the molecule transformed into the lab frame by the appropriate rotation matrix.¹⁹ The absorption dot product in the integrand depends implicitly on the laser probe direction \hat{k}_{laser} .

In the high- J limit, \mathbf{J} is treated classically as a continuous vector and is allowed any continuous projection along the coordinate axes. Thus, $n(\theta)$ is the expansion of the distribution of molecular orientations along the symmetry axis in terms of even Legendre moments,

$$n(\theta) = a_0 + a_2 P_2(\cos\theta) + a_4 P_4(\cos\theta) + \dots \quad (4.3)$$

where θ is the angle between \mathbf{J} and Z_{lab} . The $\langle \rangle$'s in Eq. (4.2) denote an average of the fast molecular rotation of the dipole axis. Because the classical molecular period of rotation, T_{rot} , is much smaller than the average fluorescence lifetime (T_{rot} is approximately 0.52 ps for $J = 15$, corresponding to about 120,000 rotations per fluorescence lifetime), the dot products corresponding to photon absorption and emission are averaged separately (incoherently), assuming no phase correlation

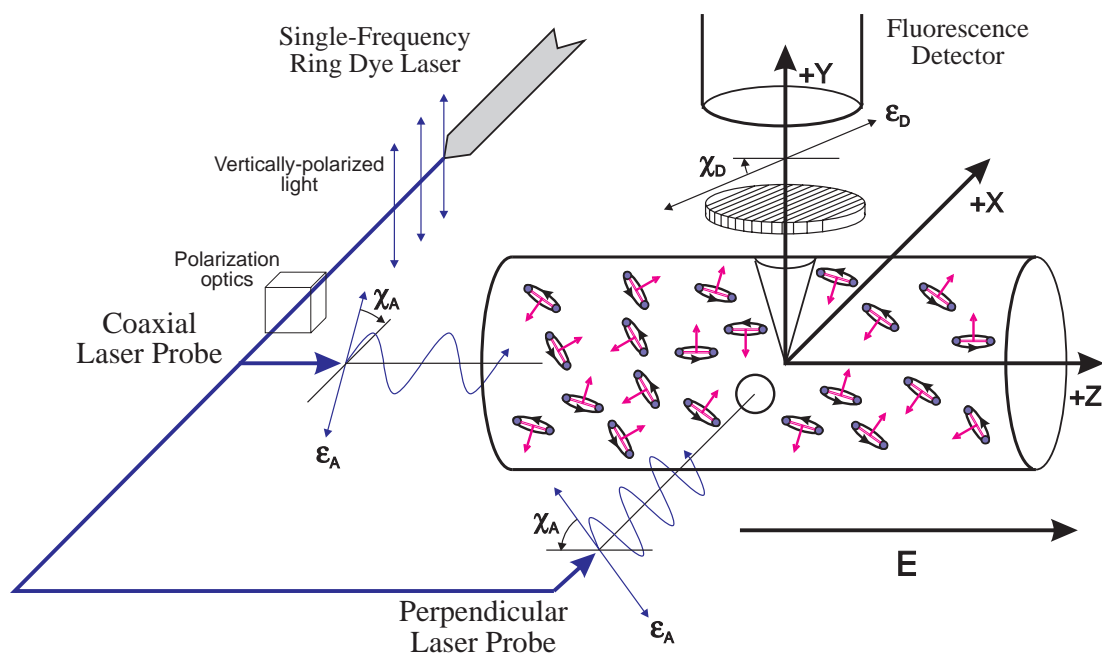


Fig. 4.3: Schematic of "two-angle" LIF geometry for alignment experiment.

between these processes; i.e., many molecular rotations are assumed to take place between absorption and emission.

The a_2 and a_4 terms are the alignment parameters of the ensemble. The expansion of Eq. (4.3) is in Legendre polynomials $P_k(\cos\theta)$ instead of spherical harmonics $Y_{kq}(\theta, \phi)$ because of the cylindrical symmetry of the experiment about the external electric field. Since the ensemble is invariant to rotations about Z_{lab} , the ϕ dependence is ignorable. Only even moments appear because we are concerned with an aligned (“double-headed arrows”) as opposed to an oriented (“single-headed arrows”) ensemble. Physically, this is due to the interaction potential being sensitive only to the angle the N_2^+ internuclear axis makes with the N_2^+ -He collision axis. Although, mathematically, the expansion of Eq. (4.3) continues past $k = 4$, in a 1+1 LIF experiment (1 photon in absorption, 1 photon in emission), it is only possible to obtain the $k = 2$ and $k = 4$ terms of this expansion. Qualitatively, this can be seen from inspection of Eq. (4.2). Loosely, each $\hat{\epsilon} \cdot \hat{\mu}$ dot product in the integral has a $\cos^2 \theta$ or $P_2(\cos\theta)$ “character”. The product of these two terms can give an expression with at most $\cos^4 \theta$ or $P_4(\cos\theta)$ character. By the orthogonality of Legendre polynomials, any expansion term of $n(\theta)$ past $k = 4$ will vanish in the integral over θ . In words, each probe or fluorescence photon carries “one moment’s worth” of information about the ensemble. Thus, in a one-photon absorption experiment, it is only physically possible to obtain the second moment of the m_J distribution. The a_2 and a_4 parameters describe the relative amounts of $P_2(\cos\theta)$ and $P_4(\cos\theta)$ needed to

characterize the underlying m_j distribution. For a bowed-down m_j distribution as shown in Fig. 4.2, a_2 is negative simply because mathematically, $+P_2(\cos\theta)$ functions happen to bow up.

A straightforward but somewhat tedious calculation²⁰ produces the result for the coaxial probe geometry as

$$\begin{aligned}
 I_{LIF}(\chi_A, \chi_D; \hat{k}_{laser} \parallel Z) = & \\
 & \frac{4\pi}{9} K \left[a_0 \left\{ 1 + \frac{3}{20} \left(-\frac{2}{3} P_2(\cos \chi_D) + \sin^2 \chi_D \cos 2\chi_A \right) \right\} \right. \\
 & + \left(\frac{2}{5} a_2 \right) \frac{1}{28} \left\{ 7 - 16 P_2(\cos \chi_D) - 3 \sin^2 \chi_D \cos 2\chi_A \right\} \\
 & \left. + \left(\frac{1}{9} a_4 \right) \frac{9}{140} \left\{ -4 P_2(\cos \chi_D) + \sin^2 \chi_D \cos 2\chi_A \right\} \right] \quad (4.4a)
 \end{aligned}$$

and for the perpendicular probe geometry,

$$\begin{aligned}
 I_{LIF}(\chi_A, \chi_D; \hat{k}_{laser} \parallel X) = & \\
 & \frac{4\pi}{9} K \left[a_0 \left\{ 1 + \frac{3}{20} \left(\frac{4}{3} P_2(\cos \chi_D) P_2(\cos \chi_A) - \sin^2 \chi_D \sin^2 \chi_A \right) \right\} \right. \\
 & + \left(\frac{2}{5} a_2 \right) \left\{ \begin{aligned} & -\frac{1}{2} P_2(\cos \chi_D) - \frac{1}{2} P_2(\cos \chi_D) \\ & + \frac{3}{28} \left(\frac{4}{3} P_2(\cos \chi_D) P_2(\cos \chi_A) + \sin^2 \chi_D \sin^2 \chi_A \right) \end{aligned} \right\} \\
 & \left. + \left(\frac{1}{9} a_4 \right) \frac{9}{140} \left\{ 8 P_2(\cos \chi_D) P_2(\cos \chi_A) - \sin^2 \chi_D \sin^2 \chi_A \right\} \right] \quad (4.4b)
 \end{aligned}$$

These two expressions correspond to Eq. (21) of Ref. 21, with the replacements:

$$A_0^{(0)} = a_0 = 1 \quad A_0^{(2)} = \frac{2}{5} a_2 \quad A_0^{(4)} = \frac{1}{9} a_4 \quad (4.5)$$

It should be noted that even in the $J \rightarrow \infty$ limit, it is necessary to choose the correct absorption and emission branches consistent with the geometry of the molecule (i.e., $P \uparrow$ or $R \uparrow$, $P \downarrow$ or $R \downarrow$ for this case) in order to obtain this correspondence.

In this “two-angle” experiment in which both (χ_A, χ_D) can be varied, the basic experimental parameter is modified from Eq. (4.1) to become

$$P(\chi_A) = \frac{I_{LIF}(\chi_A, \chi_D = 0^0) - I_{LIF}(\chi_A, \chi_D = 90^0)}{I_{LIF}(\chi_A, \chi_D = 0^0) + I_{LIF}(\chi_A, \chi_D = 90^0)} \quad (4.6)$$

with $\chi_A = 90^0$ corresponding to vertically-polarized light for either probe direction. It should be mentioned that the polarization coefficients as defined here differ from some literature,²² in which the polarization vector of the probe beam is taken as the quantization axis. In the latter designation, I_{\parallel} and I_{\perp} denote fluorescence polarized parallel and perpendicular to $\hat{\epsilon}_A$, which is only in agreement with the definitions of this work for the perpendicular laser probe $P(\chi_A = 0^0)$'s.

Figures 4.4 (a) and (b) shows plots of Eqs. (4.4) both for the case of no alignment ($a_2 = a_4 = 0$) and for a significant degree of alignment representative of the parameters observed in this experiment. It is useful to think of the two-angle experiment as producing fluorescence surfaces as in the figure that are modulated by the alignment parameters of the ensemble. Note that even for the isotropic case, the LIF surfaces are in general not flat, i.e., there exists isotropic polarization. However, note that there is a “valley” along $\chi_A = 90$ degrees in these plots for either probe direction, corresponding to the measurement scheme used here. For an isotropic distribution, this valley is perfectly flat, indicating that true polarization coefficients

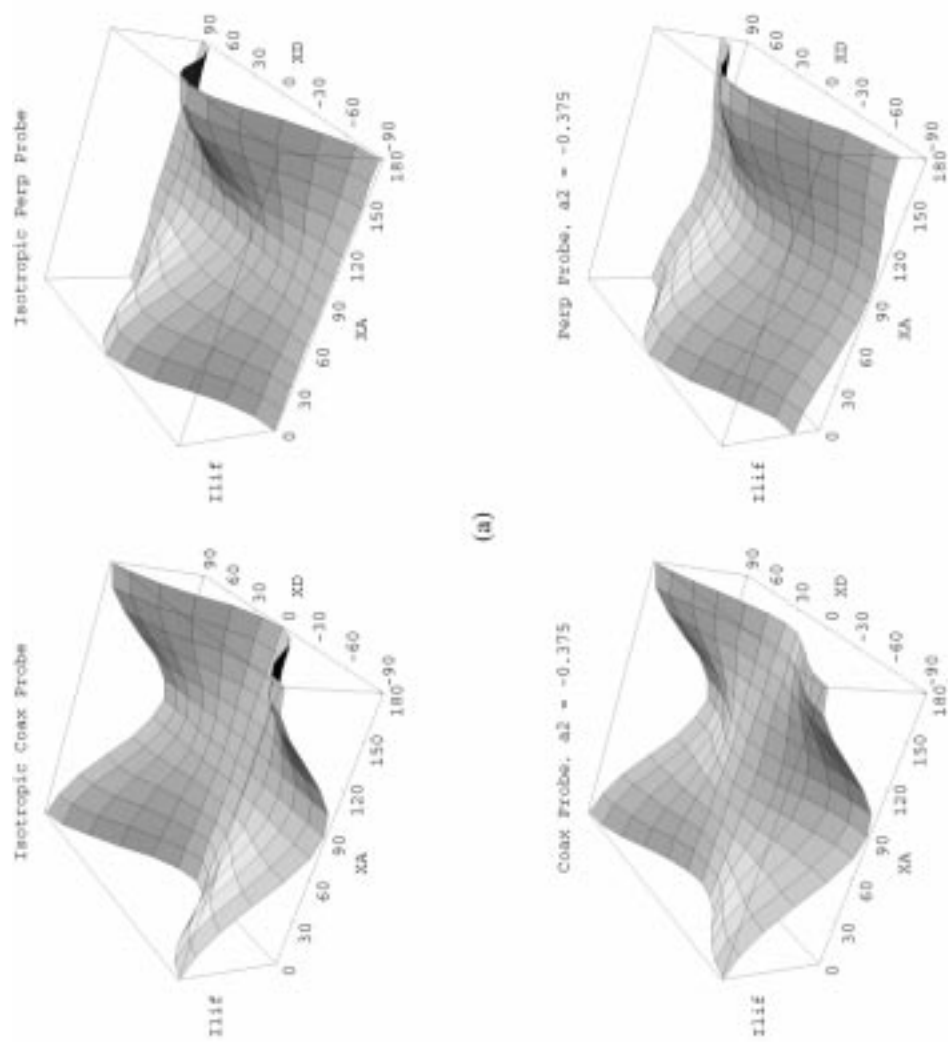


Fig. 4.4: Isotropic and aligned fluorescence intensity plots for the two probe directions.

$P(\chi_A = 90^0)$ will vanish for either probe direction. For horizontally polarized light, this model gives a value for isotropic $P(\chi_A = 0^0)$'s for the (coaxial/perpendicular) probe geometry of $(-/+)$ $1/7 \cong (-/+)$ 14.3% , a well-known result in the high-J limit. Figure 4.4 also illustrates why a measurement scheme frequently employed in absorption and TOF experiments, namely the modulation of the laser polarization angle by a photo-elastic modulator (PEM) or other device, will not work for a right-angle detection LIF experiment. One will detect a large change in fluorescence intensity (isotropic polarization) simply due to geometric factors, while the true alignment signal due to nonzero alignment will be a small signal on top of this.

3. *Quantum theory*

The model of the previous section does not account for the quantization of angular momentum nor does it conserve the angular momentum of the absorbed and emitted photons. A proper quantum-mechanical treatment of detection and characterization of molecular alignment via LIF has been previously developed in detail in two papers by Greene and Zare.^{21,23} The resulting LIF intensity expression for a known (J_i, J_e, J_f) initial, excited, and final state pump-fluoresce transition as a function of the two angles (χ_D, χ_A) shown in Fig. 4.3 is

$$I_{LIF}(\chi_D, \chi_A; \hat{k}_{laser}) = C S \sum_{\substack{k_D, k_A \\ k}} \varepsilon(k_D, k_A, k; \hat{k}_{laser}) \omega(k_D, k_A, k; J_i, J_e, J_f) A_0^{(k)} \quad (4.7)$$

where the various terms in Eq. (4.7) are defined below. Conceptually, this expression is produced from an expression analogous to Eq. (4.2) above. The absorption and

emission dot products are now replaced by amplitudes $\langle J_e m_e | \hat{\epsilon}_A \cdot \hat{\mu} | J_i m_i \rangle$ and $\langle J_f m_f | \hat{\epsilon}_D \cdot \hat{\mu} | J_e m_e \rangle$. The unknown ground-state distribution of molecular alignments $f(m_{J_i})$ is still being averaged over; however, because of the coherent sum over the indistinguishable intermediate states m_{J_e} and the incoherent sum over final states m_{J_f} , the math needed to disentangle this dynamical information from the geometrical factors becomes considerably more complicated.²¹

The various terms in Eq. (4.7) correspond to the various aspects of this model that must be accounted for. The rescaling constant C contains the experimental dependencies on ion number density, laser power, and fluorescence detection efficiency. The isotropic line strength factor S varies as the product of two dipole reduced matrix elements $\left| \langle J_f \| r^{(1)} \| J_e \rangle \langle J_e \| r^{(1)} \| J_i \rangle \right|^2$. These two factors, which are important for extracting actual alignment parameters from experimental data, are discussed in greater detail in Sec. IV.B.4 below. The $\epsilon(k_D, k_A, k; \hat{k}_{laser})$ are polarization tensor elements dependent on the values of the photon multipole moments k and completely specified by the LIF geometry, and can be shown to be identical to those in Eqs. (4.4) above. The $\omega(k_d, k_a, k; J_i, J_e, J_f)$ are angular momentum recoupling factors dependent on both the photon multipoles and the specific pump-fluoresce transition. Explicit expressions for both the polarization tensor elements and the angular momentum recoupling factors are tabulated in Ref. 21 and will not be repeated here. The angular momentum recoupling factors can be

calculated in a number of ways, including by *Mathematica*. An angular momentum calculator program written in object Pascal for the MS *Windows* environment is given in Appendix C that will calculate numerical values for these factors directly.

The $A_0^{(k)}$ are the unknown alignment parameters of the system. In general, the alignment parameters $A_q^{(k)}$ are related by a rescaling factor to the ensemble average of the spherical tensor operators $J_q^{(k)}$. The cylindrical symmetry of the experiment forces all moments with $q \neq 0$ to vanish, while the reflection symmetry requires all odd k moments to be zero. Additionally, the 1+1 photon LIF scheme constrains the photon multipole moments k_D and k_A to have only the values 0 or 2. Thus, Eq. (4.7) contains only two unknowns: $A_0^{(2)}$ and $A_0^{(4)}$, the quadrupole and hexadecapole alignment parameters, respectively. The $A_0^{(0)}$ parameter is identically equal to 1 and is usually grouped with the C prefactor and taken as a measure of total population. In general, the limits on the nonisotropic parameters are

$$-1 \leq A_0^{(2)} \leq +2 \quad \text{and} \quad -\frac{3}{7} \leq A_0^{(4)} \leq +1, \quad (4.8)$$

although the extreme values are rarely encountered in collision-induced rotational alignment experiments, and these parameters are not truly independent at these limiting values.

An approximate m_j distribution may be found from these alignment parameters. In general, the m_j distribution can be found from the state multipole expansion of the density matrix.²⁴ In this particular experiment, the density matrix is diagonal because for a cylindrically symmetric system, no coherences are possible.

The state multipoles are proportional to the alignment parameters $A_0^{(k)}$ such that the density matrix may be expanded as²⁵

$$\rho_{MM}^J = \sum_k (-1)^{J-M} \frac{(2k+1) [J(J+1)]^{k/2}}{c(k) \langle J \| J^{(k)} \| J \rangle} \begin{pmatrix} J & J & k \\ M & -M & 0 \end{pmatrix} A_0^{(k)} \quad (4.9)$$

where the expression in parentheses is a Wigner 3-j symbol. For even k , the rescaling constants $c(k)$ and reduced matrix elements $\langle J \| J^{(k)} \| J \rangle$ are^{22,25}

$$\begin{aligned} c(0) &= 1 & c(2) &= \sqrt{6} & c(4) &= \sqrt{35/8} \\ \langle J \| J^{(0)} \| J \rangle &= \sqrt{2J+1} & \langle J \| J^{(2)} \| J \rangle &= \sqrt{\frac{J(J+1)(2J-1)(2J+1)(2J+3)}{6}} \\ \langle J \| J^{(4)} \| J \rangle &= \sqrt{\frac{(J-1)J(J+1)(J+2)(2J-3)(2J-1)(2J+1)(2J+3)(2J+5)}{70}} \end{aligned} \quad (4.10)$$

The diagonal elements of the density matrix give the probability $p(J, m_J)$ of finding a molecule with angular momentum J in a given m_J state. Thus, an approximate measure of the resulting m_J distributions can then be produced from the $k = 0$ and $k = 2$ terms of Eq. (4.9); explicitly, these first two terms give:

$$p(J, m_J) = \rho_{MM}^J = \frac{1}{2J+1} + 5 \frac{3(m_J)^2 - J(J+1)}{(2J+3)(2J+1)(2J-1)} A_0^{(2)} \quad (4.11)$$

This expression is used to produce m_J distributions for the experimental data below.

4. Extensions to quantum theory

As is the usual practice in LIF experiments of this nature, particularly those with inherently low signal-to-background, all fluorescence branches from the upper electronic state are collected unresolved. This fluorescence is weighted by both the appropriate intrinsic branch-weighting (Honl-London) factors and the transmission of

any frequency-selective elements through which the fluorescence passes. As discussed in Sec. II.D, both the P and R fluorescence branches are collected here, but the interference filter used favors the P -branch over the R -branch by a factor that is approximately 9:1, depending on the particular transition probed.

The mathematical treatment of the branch-weighting is straightforward. A fluorescence intensity expression in the form of Eq. (4.7) can be written for each fluorescence branch. Assuming no J-scrambling collisions in the upper excited state, the total observed fluorescence intensity is just the sum of these two intensities

$$\begin{aligned}
 I_{Total} &= I_{P\downarrow} + I_{R\downarrow}, \text{ where} \\
 I_{P\downarrow} &= C_{P\downarrow} S_{P\downarrow} \sum_k A_0^{(k)} \epsilon(\vec{k}) \omega(\vec{k}; \vec{J}_{P\downarrow}) \\
 I_{R\downarrow} &= C_{R\downarrow} S_{R\downarrow} \sum_k A_0^{(k)} \epsilon(\vec{k}) \omega(\vec{k}; \vec{J}_{R\downarrow})
 \end{aligned} \tag{4.12}$$

where the shorthand notation $\epsilon(k_D, k_A, k; \hat{k}_{laser}) \equiv \epsilon(\vec{k})$ and $\omega(k_D, k_A, k; J_i, J_e, J_f) \equiv \omega(\vec{k}; \vec{J})$ has been employed for the arguments of the polarization tensor elements and angular momentum coupling factors. If we take the rescaling constant C and line strength factor S in Eq. (4.7) as²⁶

$$C = K [n_{ion}] [I_{i \rightarrow e}^{laser}] (\bar{\nu}_{e \rightarrow f})^3 T_{filter}(\bar{\nu}_{e \rightarrow f}), \quad S = \left| \langle J_f \| r^{(1)} \| J_e \rangle \langle J_e \| r^{(1)} \| J_i \rangle \right|^2 \tag{4.13}$$

where K is an apparatus proportionality constant, $[n_{ion}]$ is the local ion number density in the LIF region, $I_{i \rightarrow e}^{laser}$ is the laser irradiance, $\bar{\nu}_{e \rightarrow f}$ is the fluorescence transition frequency, and T_{filter} the transmission of the interference filter at this frequency. The cubed dependence on the fluorescence frequency comes from the Breit

formula²⁶ and is ultimately related to the frequency dependencies of the Einstein A and B coefficients. The product CS for the P -branch fluorescence can then be written

$$C_{P\downarrow} S_{P\downarrow} = K [n_{ion}] [I_{i\rightarrow e}^{laser}] \left| \langle J_e \| r^{(1)} \| J_i \rangle \right|^2 \times \left(\overline{\nu}_{e\rightarrow f}^P \right) T_{filter} \left(\overline{\nu}_{e\rightarrow f}^P \right) \left| \langle J_f^P \| r^{(1)} \| J_e \rangle \right|^2 \quad (4.14)$$

with an analogous expression for the R -branch. Noting that the first line of Eq. (4.14) just depends on factors related to the pump ($i \rightarrow e$) step, which is common to both branches, we can redefine the proportionality constant C as

$$C = K [n_{ion}] [I_{i\rightarrow e}^{laser}] \left| \langle J_e \| r^{(1)} \| J_i \rangle \right|^2 \quad (4.15)$$

and define effective line strength factors S_P and S_R by the second line of Eq. (4.14),

$$S_P = \left(\overline{\nu}_{e\rightarrow f}^P \right) T_{filter} \left(\overline{\nu}_{e\rightarrow f}^P \right) \left| \langle J_f^P \| r^{(1)} \| J_e \rangle \right|^2 \quad (4.16)$$

$$S_R = \left(\overline{\nu}_{e\rightarrow f}^R \right) T_{filter} \left(\overline{\nu}_{e\rightarrow f}^R \right) \left| \langle J_f^R \| r^{(1)} \| J_e \rangle \right|^2$$

such that the total branch-weighted fluorescence is given by

$$I_{Total} = C S_P \sum_k A_0^{(k)} \varepsilon(\vec{k}) \omega(\vec{k}; \vec{J}_{P\downarrow}) + C S_R \sum_k A_0^{(k)} \varepsilon(\vec{k}) \omega(\vec{k}; \vec{J}_{R\downarrow}) \quad (4.17)$$

with the branch-weighting given by the effective line strength factors in Eq. (4.16).

The fluorescence branch-weighting is just an experimental complication and no approximations have been made. However, as is often done in alignment experiments, the measured polarizations are converted into quadrupole alignment parameters $A_0^{(2)}$ in the approximation that the hexadecapole alignment parameter $A_0^{(4)}$ is negligible (i.e., set to zero in Eq. (4.7) or (4.17)). Pragmatically, this is necessary because only one experimental unknown can be extracted from a linear

polarization coefficient of the form of Eq. (4.6). Physically, for the relatively high ($J>9$) rotor states studied in this work, it would be expected that $A_0^{(2)} > A_0^{(4)}$. This intuition is supported by the CC calculations of Follmeg on N_2^+ -He.¹² These calculations show that the $K=4$ tensor cross sections (discussed below), which are associated with the hexadecapole parameter, are at least an order of magnitude smaller than the $K=2$ tensor cross sections associated with the quadrupole parameter for all states studied. Thus, we believe for this particular set of experiments that the dominant moment approximation is a very good one.

Given this approximation, it is straightforward to produce an explicit formula for quadrupole alignment parameters as a function of measured polarizations. The assumption is made throughout that a point fluorescence source is being imaged, the probe-detection geometry is perfectly rectilinear, and the angles (χ_D, χ_A) are perfectly matched to the apparatus geometry. We note in passing that none of these assumptions are realized in the practice of this experiment! Setting $A_0^{(4)}$ identically equal to zero in Eq. (4.7) yields the result

$$A_0^{(2)} = \frac{\{D_{\parallel}^{(0)} + D_{\perp}^{(0)}\} P}{\{D_{\parallel}^{(2)} - D_{\perp}^{(2)}\} - \{D_{\parallel}^{(2)} + D_{\perp}^{(2)}\} P} \quad (4.18)$$

with the definitions:

$$\begin{aligned} D_{\parallel}^{(0)} &= \varepsilon_{\parallel}(0,0,0) \omega(0,0,0; \vec{J}) + \varepsilon_{\parallel}(2,2,0) \omega(2,2,0; \vec{J}) \\ D_{\parallel}^{(2)} &= \varepsilon_{\parallel}(2,0,2) \omega(2,0,2; \vec{J}) + \varepsilon_{\parallel}(0,2,2) \omega(0,2,2; \vec{J}) + \varepsilon_{\parallel}(2,2,2) \omega(2,2,2; \vec{J}) \end{aligned} \quad (4.19)$$

where the subscript on the polarization tensor elements denotes the setting of the fluorescence polarizer angle χ_D either parallel or perpendicular to the drift tube axis.

The $D_{\perp}^{(k)}$ terms are defined analogously. Equation. (4.18) is the one-branch fluorescence expression in the dominant moment approximation. For weighted fluorescence branches, each term in braces in Eq. (4.18) appears twice, once for each fluorescence branch, and is weighted by the effective line strength factors of Eq. (4.16). This two-branch expression is the formula used below to calculate $A_0^{(2)}$'s from corrected polarizations.

Another experimental complication is spin depolarization. As discussed in Sec. II.G, N_2^+ possesses nonspatial angular momentum vectors associated with the unpaired electronic spin \mathbf{S} and coupled nuclear spins \mathbf{I} ; these spins lead to a degradation or depolarization of the degree of observed alignment of the total orbital angular momentum \mathbf{N} . This is because the addition of the electronic and nuclear spins to the total orbital angular momentum means that both \mathbf{N} and \mathbf{J} precess about \mathbf{F} , which remains space-fixed in the lab frame. The spins interact very weakly with the scattering potential, so they do not become aligned in collisions with the He buffer.

However, it is possible to correct the alignment parameters for the spin depolarizations. There are several conventional formulas in the literature. Here, we correct for the depolarization of the nuclear spins only to obtain the true alignment of \mathbf{J} . Specifically, each quadrupole alignment moment derived from a measured polarization according to Eq. (4.18) is corrected as:

$$\bar{g}^{(2)} A_0^{(2)}_{\text{actual}} = A_0^{(2)}_{\text{observed}} \quad (4.20)$$

with the correction factor $\bar{g}^{(2)}$ given by:²¹

$$\bar{g}^{(2)} = \sum_{F_i} \frac{(2F_i + 1)^2}{2I + 1} \left\{ \begin{matrix} F_i & F_i & 2 \\ J_i & J_i & I \end{matrix} \right\}^2 \quad (4.21)$$

where the expression in braces is a Wigner six-j symbol and the sum is over all unresolved hyperfine levels. Since the LIF measurements are time-unresolved (cw) and since the linewidth of the laser is sufficiently narrow that coherent excitation of the unresolved hyperfine levels is not possible, this correction is applied to the LIF absorption step only. The $\bar{g}^{(2)}$ factors approach unity fairly rapidly with increasing J, as would be anticipated from the vector model. For the R₁(15) transition, Eq. (4.21) gives $\bar{g}^{(2)} = 0.984$, and the lowest J-state probed here, J=9.5, has $\bar{g}^{(2)} = 0.960$. Thus, this correction is essentially negligible at the level of detail of the current measurements. We do note that for sub-Doppler probing, there is an argument that Eq. (4.21) should be modified to include a factor $w(F_i)$ in the summation that weights each term in the sum by the relative strength of each sub-Doppler hyperfine component at the given detuning. However, this approach was not explored.

C. Experimental & analysis techniques

As made clear in Sec. IV.B.3 above, in principle the two unknown alignment parameters $A_0^{(2)}$ and $A_0^{(4)}$ could be determined by measuring the LIF intensity at a grid of different angles (χ_A, χ_D) and then performing a linear least-squares fit. Additionally, if one is primarily interested in determining the dominant quadrupole alignment parameter, data in principle could be taken at the set of special angles (χ_A, χ_D) that force the geometrical coefficient $\varepsilon(k_D = 2, k_A = 2, k = 4; \hat{k}_{laser})$ of the

$A_0^{(4)}$ term to zero. This so-called “magic line” experiment²¹ yields a fluorescence measurement that is perfectly free of contributions from hexadecapole alignment.

Unfortunately, in experimental practice matters are not so tidy. Although this grid approach is explored below in Sec. IV.D, we believe this is not the most robust method for acquiring data on this experiment. There are several important pragmatic difficulties. For one, both long and short term fluctuations in ion density and ring dye laser power make comparison of polarization curves with more than a few points difficult. Additionally, for an arbitrary choice of angles (χ_A, χ_D) , a significant component of the polarized fluorescence will be due to isotropic polarization. However, the largest problem is that there remain unresolved systematics in the experiment. The spurious polarization systematics, discussed in Sec. IV.E, make a precise determination of the absolute value of alignment parameters very difficult. In practice, we found the best data were always obtained by comparing relative values of $P(\chi_A = 90^\circ)$'s as a function of laser detuning.

There are several advantages to this approach. As discussed above in Sec. IV.B, this scheme is in principle free of isotropic polarization contributions. Also, the linear polarization coefficients have a very simple interpretation: a true $P(\chi_A = 90^\circ)$ of zero indicates no rotational alignment, while true positive (negative) polarization coefficients are associated with negative (positive) quadrupole alignment parameters, which in turn indicate a preference for the rotational angular momentum vectors to be aligned perpendicular (parallel) to the field axis. Only two angles of measurement are needed to obtain a data point, which greatly speeds the data acquisition, and the 0 and

90 degree polarizer settings measure the extremes of the fluorescence polarization, permitting the general trends of the experiment to be mapped out quickly. Additionally, long-term fluctuations in ion density and laser power tend to be canceled out by rapid, comparative $0^0/90^0$ measurements. The primary disadvantage of this method is that the higher-order hexadecapole moment $A_0^{(4)}$ must be neglected (i.e., set to zero) in order to obtain an $A_0^{(2)}$ quadrupole moment for each polarization coefficient, as discussed in Sec. IV.B.4 above. However, an approach frequently employed here is to ignore these underlying alignment parameters and treat the measured polarizations on a purely phenomenological level. Indeed, it can be argued that since there are unresolved systematics in this experiment, the measured polarizations should be regarded as the fundamental entities, and only relative comparisons between these polarizations are valid. For the relatively high J states studied here, this is a very reasonable approximation.

The mechanics of acquiring sub-Doppler polarization data are now discussed. The “atom” of data collection is the counting *trial*, which is a measurement of polarized LIF acquired at a specific laser detuning, with a specific fixed setting of polarizer angles (χ_A, χ_D) for a given interval of time. For the above scheme, two trials with $\chi_A = 90^0$ and χ_D set sequentially to 0 and 90 degrees are needed to measure a $P(90^0)$. The trials are acquired at sub-Doppler laser detunings referred to in general as *markers*, even though, as discussed below, there may not be a physical marker at the chosen detuning. Trials are assembled together into *sequences*, which are designed to yield a certain number of polarization coefficients (or more generally,

polarization curves) for each marker. Sequences are run for one or more *iterations* before the trial data is written out to disk. *Calibration files* used to determine marker positioning are taken before and sometimes after the sub-Doppler data acquisition.

The choice of the best sequences for a given situation was determined by experience. In principle, the sequences can be of arbitrary length and complexity, involving many sub-Doppler markers with trial lengths of varying time duration. In practice, it was found best to keep things as simple as possible. The trial counting intervals were kept short to insure good time correlation between successive measurements. The longest trials used for any sub-Doppler experiment were 20 s. Additionally, although not necessary (and indeed, not optimal), the trials were the same length throughout the sequence. The sequences were kept fairly short to insure that the ring dye laser did not drift significantly in frequency or mode-hop; the longest sequences used consisted of 29 trials. In a single sequence, data were acquired at only one, two or three positions (referred to as signal or “A” markers) on a given Doppler profile, as well as one background position (“B” marker) at least 3.7 GHz (typically considerably more) from line center. The 2A/B and 3A/B sequences were employed about line center to interleave low-frequency and high-frequency trials, and to insure equivalent counting statistics for each marker. The 1A/B sequences were either used to acquire data in the wings of the line profiles or for diagnostic checks at line center.

Table 4.1 is an example of a 29-trial, 3A/B sequence which yields four polarization coefficients for each marker, for each iteration. In practice, it was found essential to “mix up” the trials and sequences to insure that one particular polarizer setting or marker is not being systematically favored. In particular, sequences must be

<i>Trial</i> #	A Marker 0 χ_D	A Marker 1 χ_D	A Marker 2 χ_D	B Marker 3 χ_D	Trial Description
1	0				Total polarized LIF signal
2	90				"
3	90				"
4	0				"
5		270			"
6		0			"
7		0			"
8		270			"
9			0		"
10			90		"
11			90		"
12			0		"
13				0	LIF effective background
14				90	LIF effective background
15	270				Total polarized LIF signal
16	0				"
17	0				"
18	270				"
19		0			"
20		90			"
21		90			"
22		0			"
23			270		"
24			0		"
25			0		"
26			270		"
27				270	Flowing afterglow
28				0	fluorescence check
29				0	PMT dark count

Table 4.1: Example of actual data collection sequence used for sub-Doppler alignment experiments. This is a “3A/B” sequence consisting of three signal (A) markers (numbered 0,1 2) and a background (B) marker (3). The 270 degree trials are treated as equivalent to 90 degrees and are taken to reduce wear on the rotation stage. The “mirror” sequence consists of just exchanging the 0 and 90 degree trials.

arranged so that there are equal numbers of pairs of first, 0 degree, then 90 degree (0/90) measurements and 90/0 measurements. Additionally, “mirror” sequences are run in which the order of the 0/90 and 90/0 trials pairs are interchanged. These measures are necessary primarily because of the overall downward slope of the LIF signal with time, due to both losses in both laser power and ion density. Alternations in the polarization coefficients can often be seen which will correlate with this systematic.

Two techniques were used to position the ring dye laser in frequency space. The simplest method was just to designate positions by their digital-to-analog (D/A) setting. These so-called “software” frequency signal markers were set symmetrically about the onscreen A cursor in the data acquisition program (Eta-Spex) by a pre-selected digital-to-analog delta value; the B marker was set at the B cursor position. In the sub-Doppler trials, the ring laser was slewed at a preset rate to these D/A positions. Although more uncertain than hardware positioning, this technique was often good enough for acquiring diagnostic or plasma data, where the relative detuning from line center was not particularly critical. The second method was to use the 0.375 GHz free spectral range transmission peaks of the 20 cm ULE cavity as frequency markers, as discussed in Sec. II.C.2 above. The spacing of these “hardware” markers turns out to be quite appropriate for this experiment.

The relative detuning from line center was determined by taking an unpolarized calibration file immediately before the trial data. However, for the data acquired with the stepper motor rotation stage in the latter part of this work, a slightly different analysis technique was used. Because the polarizer was fixed in the stage

and could not be removed, a second unpolarized PMT channel was added to the bottom of the apparatus to allow for a better fit of the unpolarized calibration scan. Calibration files were taken both immediately before and after the trial data. The detunings were determined by fitting these unpolarized PMT signals to a 3-parameter Gaussian and then determining the average frequency marker position relative to line center. Frequency error bars could then be assigned by taking the difference between these positions.

For each trial, data from three 16-bit microcomputer-controlled counters are acquired. One counter accumulates the polarized fluorescence PMT signal. A second counter integrates a measure of “local” ring dye laser power during the trial, obtained from the normalization photodiode of the cavity-side lock system; a third counter records a count of laser unlock/lock transitions during the trial for diagnostic purposes. Both of these technical details are discussed in more depth in Sec. II.C. As discussed in Sec. II.E, the counters are hardware-gated by a crystal-locked trial gate generated by another counter. The counters are sampled at either 0.5 s or 1.0 s intervals, depending on gate width, and an average and sample standard deviation are calculated from these samples before they are discarded. A large standard deviation in the counting rate of either the PMT or ring dye laser power signal is usually an indication that something has gone amiss during the trial.

Acquisition program (Eta-Spex) output of typical trial data for a 2A/B sequence is shown in Table 4.2. Three sub-tables are contained in the output. The marker table, indexed by marker number, contains information about where the sub-Doppler markers fall in frequency space. The trial information table, indexed by trial

Eta-Spex Vers. 1.62: file format vers. 0.78

Acquisition beginning: 11:29pm Sat 28 Feb 1998
 Calibration file = C:\SPECTRA\EBAN\2VOD792.PRN
 DIS description of sequence = R1(9) coax probe, 12 Td 2a/b middle

Marker #	Etalon Peak #	Initial Channel #	Equivalent D/A Position
0	5	108	3235
1	10	218	2355
2	21	470	339

Trial #	Xd	Xa	Gate Width (ms)	Sample T (ms)	Marker #	Description
1	0	90	16000	1000	0	Pol LIF + Pol SLL bk + FA bk + PMT bk
2	90	90	16000	1000	0	Pol LIF + Pol SLL bk + FA bk + PMT bk
3	90	90	16000	1000	0	Pol LIF + Pol SLL bk + FA bk + PMT bk
4	0	90	16000	1000	0	Pol LIF + Pol SLL bk + FA bk + PMT bk
5	0	90	16000	1000	0	Pol LIF + Pol SLL bk + FA bk + PMT bk
6	90	90	16000	1000	0	Pol LIF + Pol SLL bk + FA bk + PMT bk
7	270	90	16000	1000	1	Pol LIF + Pol SLL bk + FA bk + PMT bk
8	0	90	16000	1000	1	Pol LIF + Pol SLL bk + FA bk + PMT bk
9	0	90	16000	1000	1	Pol LIF + Pol SLL bk + FA bk + PMT bk
10	270	90	16000	1000	1	Pol LIF + Pol SLL bk + FA bk + PMT bk
11	270	90	16000	1000	1	Pol LIF + Pol SLL bk + FA bk + PMT bk
12	0	90	16000	1000	1	Pol LIF + Pol SLL bk + FA bk + PMT bk
13	0	90	16000	1000	2	Pol SLL bk + FA bk + PMT bk
14	270	90	16000	1000	2	Pol SLL bk + FA bk + PMT bk
15	270	90	16000	1000	0	Pol LIF + Pol SLL bk + FA bk + PMT bk
16	0	90	16000	1000	0	Pol LIF + Pol SLL bk + FA bk + PMT bk
17	0	90	16000	1000	0	Pol LIF + Pol SLL bk + FA bk + PMT bk
18	270	90	16000	1000	0	Pol LIF + Pol SLL bk + FA bk + PMT bk
19	270	90	16000	1000	0	Pol LIF + Pol SLL bk + FA bk + PMT bk
20	0	90	16000	1000	0	Pol LIF + Pol SLL bk + FA bk + PMT bk
21	0	90	16000	1000	1	Pol LIF + Pol SLL bk + FA bk + PMT bk
22	90	90	16000	1000	1	Pol LIF + Pol SLL bk + FA bk + PMT bk
23	90	90	16000	1000	1	Pol LIF + Pol SLL bk + FA bk + PMT bk
24	0	90	16000	1000	1	Pol LIF + Pol SLL bk + FA bk + PMT bk
25	0	90	16000	1000	1	Pol LIF + Pol SLL bk + FA bk + PMT bk
26	90	90	16000	1000	1	Pol LIF + Pol SLL bk + FA bk + PMT bk
27	90	90	16000	1000	2	FA bk + PMT bk, w/ polarizer
28	0	90	16000	1000	2	FA bk + PMT bk, w/ polarizer
29	0	90	16000	1000	2	PMT dark count bk

Seq	RDL	PMT Signal [cts]		RDL power [cts]		Lock/unlock cts		V_FP	IRQ cnt	
ltr	Trial #	D/A pos(ch #)								
1	1	3254(106)	52622	3289 ± 72	30977	1936 ± 34	33	2 ± 2	6.55	17
1	2	3254(106)	55420	3464 ± 70	30764	1923 ± 21	13	1 ± 1	9.99	17
1	3	3254(106)	55000	3438 ± 61	30762	1923 ± 20	17	1 ± 1	9.96	17
1	4	3254(106)	51832	3240 ± 54	30855	1928 ± 18	19	1 ± 2	10.00	17
1	5	3254(106)	52007	3250 ± 69	30760	1923 ± 15	25	2 ± 1	10.00	17
1	6	3254(106)	54988	3437 ± 58	30681	1918 ± 18	32	2 ± 2	9.76	17
1	7	2386(214)	50617	3164 ± 74	30643	1915 ± 14	10	1 ± 1	8.85	17
1	8	2386(214)	50287	3143 ± 67	30656	1916 ± 8	18	1 ± 1	8.96	17
1	9	2386(214)	49849	3116 ± 57	30633	1915 ± 15	7	0 ± 1	9.00	17
1	10	2386(214)	51083	3193 ± 63	30644	1915 ± 15	7	0 ± 1	8.36	17
1	11	2386(214)	50044	3128 ± 54	30611	1913 ± 10	2	0 ± 1	8.09	17
1	12	2386(214)	49686	3105 ± 66	30530	1908 ± 20	10	1 ± 1	6.80	17
1	13	416(460)	5761	360 ± 21	29919	1870 ± 11	34	2 ± 2	2.99	17
1	14	416(460)	5831	364 ± 21	29903	1869 ± 12	27	2 ± 2	2.36	17
1	15	3255(106)	54385	3399 ± 69	30500	1906 ± 12	8	1 ± 1	3.08	17
1	16	3255(106)	50853	3178 ± 70	30607	1913 ± 19	15	1 ± 1	8.21	17
1	17	3255(106)	51107	3194 ± 68	30570	1911 ± 18	26	2 ± 1	7.38	17
1	18	3255(106)	54409	3401 ± 94	30357	1897 ± 20	17	1 ± 2	7.67	17
1	19	3255(106)	55211	3451 ± 55	30600	1913 ± 14	18	1 ± 1	6.73	17
1	20	3255(106)	50537	3159 ± 74	30317	1895 ± 22	9	1 ± 1	6.88	17
1	21	2385(214)	49946	3122 ± 43	30239	1890 ± 11	21	1 ± 1	2.82	17
1	22	2385(214)	49758	3110 ± 80	30298	1894 ± 14	13	1 ± 1	9.98	17
1	23	2385(214)	49661	3104 ± 52	30312	1895 ± 16	21	1 ± 1	9.78	17
1	24	2385(214)	48980	3061 ± 76	30142	1884 ± 15	19	1 ± 1	9.68	17
1	25	2385(214)	48738	3046 ± 57	30367	1898 ± 12	21	1 ± 2	9.47	17
1	26	2385(214)	50032	3127 ± 56	30341	1896 ± 13	20	1 ± 1	9.59	17
1	27	421(460)	5914	370 ± 20	29681	1855 ± 14	14	1 ± 1	6.77	17
1	28	421(460)	5414	338 ± 16	29610	1851 ± 17	12	1 ± 1	2.15	17
1	29	421(460)	4496	281 ± 18	29658	1854 ± 14	26	2 ± 2	1.60	17

Elapsed time for sequence iteration = 648 sec

Table 4.2: Example of program data output. Three sub-tables are shown: the marker table, the trial information table, and the trial data table, and are discussed in the text.

number, stores the information needed to carry out the sub-Doppler trials, and contains the marker number as a pointer to the marker table. The trial data table, indexed by the trial number, contains the actual data acquired during the sequence. The data from the three counters appears in columnar form. Under each counter heading is the total counts accumulated during the trial, average counting rate per sample interval, and the sample standard deviation (note that there are only two independent pieces of information here). Although the actual sequences used for this particular set of experiments were quite simple, it should be emphasized that the programming of an arbitrarily complex sequence is possible with this technique. The trial information tables for the various sequences are data structures stored as program look-up tables that can be easily changed. Often “programming” of a new sequence was done on the fly and the program recompiled while the experiment was running. Since the stepper motor-driven rotation stage and hardware marker positioning are completely under computer control, much of the clerical work of data acquisition is almost completely automated.

Table 4.3 illustrates the calculation of corrected polarization coefficients from trial data. This table, which is appended by the acquisition program to the data files, contains the analysis of the same data shown in Table 4.2. Two corrections are always applied to the raw polarization data. An effective background, measured at the “B” marker, is subtracted from the total accounts accumulated during the LIF trial. The three contributors to this effective background are residual scattered laser light, unquenched flowing afterglow fluorescence, and PMT dark counts, the latter being the dominant component at typically $200 \text{ counts s}^{-1}$. Flowing afterglow fluorescence

Seq	0 degree	90 degree					
Iter	Marker #	Trial #'s	Fluorescence	Fluorescence	P(90) x 100%	Comments	
1	0	1, 2	52622	55420	-2.59	No background correction	
1	2	13,14	- 5761	- 5831	-----	Subtract off effective background	
1	0*	(1-13),(2-14)	46861	49589	-2.83	Background-corrected polarization	
1	0	1, 2	÷ 30977	÷ 30764	-----	Laser power for LIF trials	
1	0*	(1 ÷ lp),(2 ÷ lp)	1.5128	1.6119	-3.17	Bkgnd & laser-power corrected P(90)	
1	0	4, 3	51832	55000	-2.97	No background correction	
1	2	13,14	- 5761	- 5831	-----	Subtract off effective background	
1	0*	(4-13),(3-14)	46071	49169	-3.25	Background-corrected polarization	
1	0	4, 3	÷ 30855	÷ 30762	-----	Laser power for LIF trials	
1	0*	(4 ÷ lp),(3 ÷ lp)	1.4931	1.5984	-3.40	Bkgnd & laser-power corrected P(90)	
1	0	5, 6	52007	54988	-2.79	No background correction	
1	2	13,14	- 5761	- 5831	-----	Subtract off effective background	
1	0*	(5-13),(6-14)	46246	49157	-3.05	Background-corrected polarization	
1	0	5, 6	÷ 30760	÷ 30681	-----	Laser power for LIF trials	
1	0*	(5 ÷ lp),(6 ÷ lp)	1.5034	1.6022	-3.18	Bkgnd & laser-power corrected P(90)	
1	0	16,15	50853	54385	-3.36	No background correction	
1	2	13,14	- 5761	- 5831	-----	Subtract off effective background	
1	0*	(16-13),(15-14)	45092	48554	-3.70	Background-corrected polarization	
1	0	16,15	÷ 30607	÷ 30500	-----	Laser power for LIF trials	
1	0*	(16 ÷ lp),(15 ÷ lp)	1.4733	1.5919	-3.87	Bkgnd & laser-power corrected P(90)	
1	0	17,18	51107	54409	-3.13	No background correction	
1	2	13,14	- 5761	- 5831	-----	Subtract off effective background	
1	0*	(17-13),(18-14)	45346	48578	-3.44	Background-corrected polarization	
1	0	17,18	÷ 30570	÷ 30357	-----	Laser power for LIF trials	
1	0*	(17 ÷ lp),(18 ÷ lp)	1.4833	1.6002	-3.79	Bkgnd & laser-power corrected P(90)	
1	0	20,19	50537	55211	-4.42	No background correction	
1	2	13,14	- 5761	- 5831	-----	Subtract off effective background	
1	0*	(20-13),(19-14)	44776	49380	-4.89	Background-corrected polarization	
1	0	20,19	÷ 30317	÷ 30600	-----	Laser power for LIF trials	
1	0*	(20 ÷ lp),(19 ÷ lp)	1.4769	1.6137	-4.43	Bkgnd & laser-power corrected P(90)	
1	1	8, 7	50287	50617	-0.33	No background correction	
1	2	13,14	- 5761	- 5831	-----	Subtract off effective background	
1	1*	(8-13),(7-14)	44526	44786	-0.29	Background-corrected polarization	
1	1	8, 7	÷ 30656	÷ 30643	-----	Laser power for LIF trials	
1	1*	(8 ÷ lp),(7 ÷ lp)	1.4524	1.4615	-0.31	Bkgnd & laser-power corrected P(90)	
1	1	9,10	49849	51083	-1.22	No background correction	
1	2	13,14	- 5761	- 5831	-----	Subtract off effective background	
1	1*	(9-13),(10-14)	44088	45252	-1.30	Background-corrected polarization	
1	1	9,10	÷ 30633	÷ 30644	-----	Laser power for LIF trials	
1	1*	(9 ÷ lp),(10 ÷ lp)	1.4392	1.4767	-1.28	Bkgnd & laser-power corrected P(90)	
1	1	12,11	49686	50044	-0.36	No background correction	
1	2	13,14	- 5761	- 5831	-----	Subtract off effective background	
1	1*	(12-13),(11-14)	43925	44213	-0.33	Background-corrected polarization	
1	1	12,11	÷ 30530	÷ 30611	-----	Laser power for LIF trials	
1	1*	(12 ÷ lp),(11 ÷ lp)	1.4387	1.4444	-0.19	Bkgnd & laser-power corrected P(90)	

Table 4.3: Example of program data analysis output, illustrating the analysis of the data shown in Table 4.2. The final background & laser-power corrected polarization coefficients are shown in bold.

is quenched by the neutral N_2 flow to approximately 40 counts s^{-1} or less. Scattered laser light is held to typically less than 20 counts s^{-1} ($120 \text{ counts s}^{-1}$) for coaxial (perpendicular) probe. Note that careful beam transport, aided by the two prealigned counterpropagating HeNe lasers, is absolutely essential to minimize this background contribution. After background subtraction, the ring dye laser power dependence of the resulting LIF signal is corrected by simple division of the accumulated trial counts in the laser power channel. Diagnostic data indicate that the LIF signal remains linear with laser power up to the absolute maximum of 50 mW at the baffle arm entrances. A linear polarization coefficient is then calculated from the background and laser-power-corrected LIF signals as per Eq. (4.6). These calculation steps are shown explicitly in Table 4.3. Polarization coefficients are calculated from raw data and background-corrected-only data for diagnostic purposes; note that the laser power correction is typically small. Since these two corrections are always applied to the data, these are referred to as “uncorrected” polarization coefficients, meaning that no additional *systematic* corrections of any sort have been applied.

D. Results

Two sets of alignment data are presented in this section, acquired in the fall of '95 and the spring of '98. The fall '95 data have been previously published²⁷ and are discussed in Sec. IV.D.1. For a variety of reasons, it was felt necessary to perform the experiment again. These first data were taken with the production conditions of Fig. 2.3, which were subsequently found to lead to a significant zero-field axial ion velocity systematic, as discussed in Sec. III.E.1. There was some residual concern that

this systematic would invalidate the alignment results. Additionally, the polarization systematics in this first experiment were not adequately resolved. In particular, there was concern that the manual rotation stage PMT stack employed in the first work was introducing systematic errors. Most importantly, several other experiments have since been conducted by other groups^{7,9} suggesting that this particular experiment is perhaps a key link to understanding partially velocity-selected collision-induced rotational alignment. Thus a second set of experiments in the spring of '98 were conducted, focusing on possible rotational state effects. These results are presented in Sec. IV.D.2.

1. Field dependence of alignment for single rotational line

The basic experimental idea was to examine partial velocity-selected alignment for a single high-lying rotational state, $R_1(N=15)$, for the two probe directions and several field strengths. Figures 4.5 (a) and (b) display these results for the three field strengths examined. All of this data were taken with the manual rotation stage PMT stack and the “software” sub-Doppler positioning scheme, with the production conditions of Fig. 2.3. There are several significant qualitative features to be explained in these data. For perpendicular probe at a fixed field strength, the polarization coefficients are essentially equal across the Doppler profile and the degree of polarization increases somewhat with increasing field strength. For coaxial probe at a fixed, non-zero field strength, the degree of polarization increases monotonically across the Doppler profile, and the slope of this increase appears to increase as well with field strength, as can be seen in Fig. 4.5 (b). Additionally, inspection of Fig. 4.5 will reveal that data points taken at the same laser detuning (i.e.,

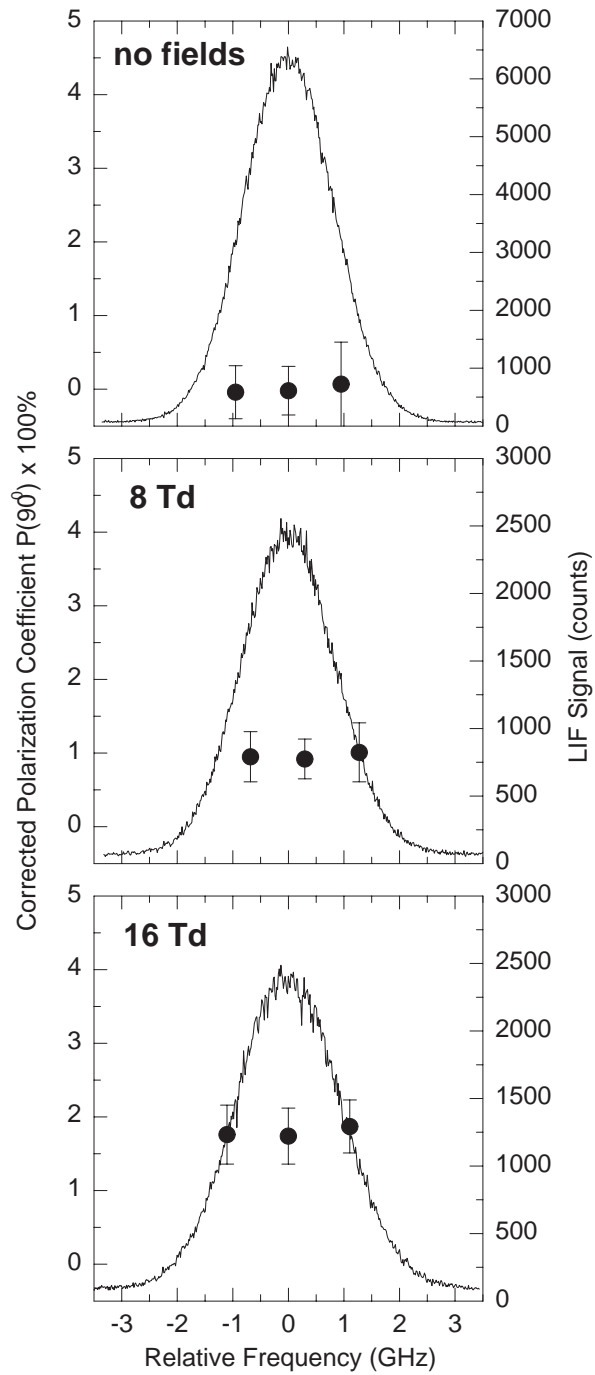


Fig. 4.5 (a): Perpendicular probe polarization results for $R_1(15)$. The corrected polarizations are shown at the approximate sub-Doppler detunings at which they were acquired.

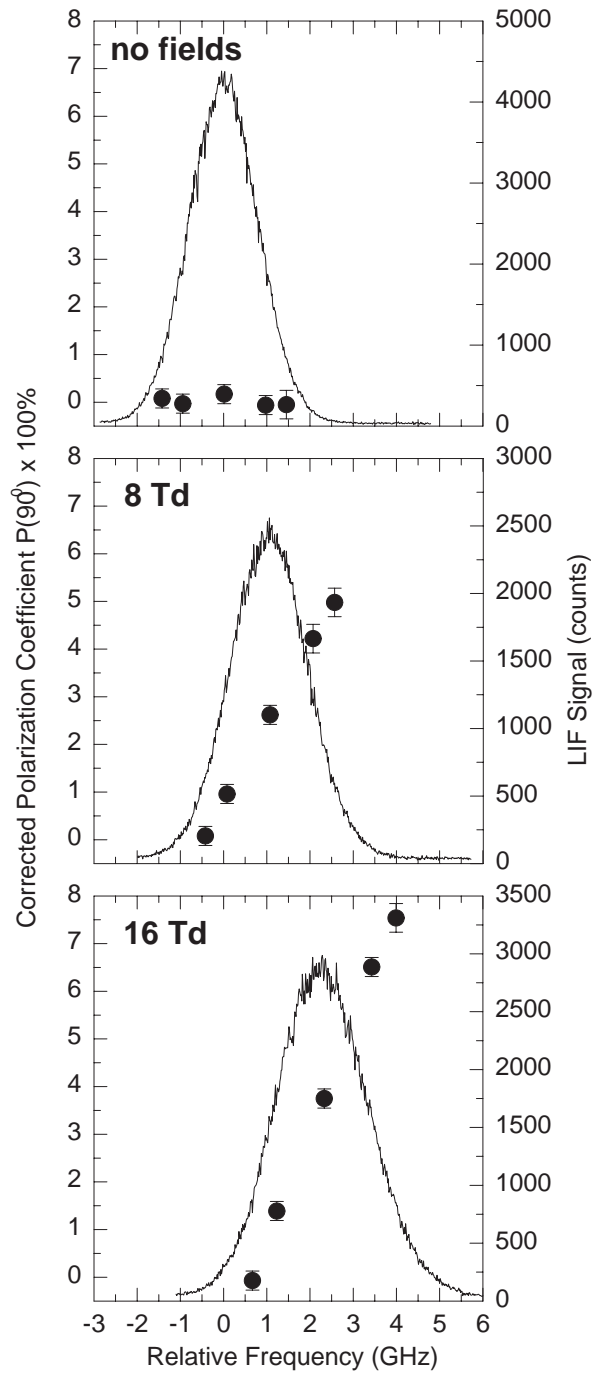


Fig. 4.5 (b): coaxial probe polarization results for $R_1(15)$. The corrected polarizations are shown at the approximate sub-Doppler detunings at which they were acquired.

absolute frequency) but at different field strengths do not in general have the same alignment.

It is important to keep in mind that the single-frequency LIF technique used in this experiment measures velocity vector projections along the laser propagation direction \hat{k}_{laser} ; ions that have laboratory velocity components along \hat{k}_{laser} in resonance with the laser frequency can absorb a photon, fluoresce, and, when in the LIF imaging region of the apparatus, be detected. As discussed in Chapter III, the result of probing in a particular direction is a steady-state velocity component distribution function, which is a projection of the complete ion velocity distribution function. If we assume that the components of the complete velocity distribution function are either completely uncorrelated or very weakly correlated and thus separable, the perpendicular and coaxial laser probe data provide two orthogonal “slices” of this distribution function. Probing perpendicular (parallel) to the drift-tube axis at a particular frequency effectively constrains the laboratory velocity component of the fluorescing molecules along \hat{k}_{laser} , while the components transverse to \hat{k}_{laser} can vary over all possible values with a distribution given by the parallel (perpendicular) velocity component distribution. Thus, a specific probe direction gives an effective average over the other, orthogonal component.

A simple qualitative explanation of the features in Fig. 4.5 can be given, using the arguments above. The anisotropy of the relative velocity vector distribution is most pronounced in the field direction. The perpendicular probe polarizations always average over these anisotropies. If the velocity distribution function is separable, these data will then be insensitive to the particular velocity vector component selected by

the laser and will be an effective average over the field direction. This would imply no variation across the Doppler profile for perpendicular probe and a fixed field strength; as the field strength is increased, the field direction anisotropy increases, and the perpendicular polarizations increase as well. Likewise, the coaxial probe polarizations average over the radial or perpendicular velocity components, but now each data point represents a velocity slice taken along the direction of greatest anisotropy. For a fixed field strength, as the laser is scanned from the low to the high-velocity tail of a coaxial Doppler profile, the relative velocity vector distribution becomes increasingly more directed, as reflected by the increasing coaxial polarizations with increasing laser frequency. Again, the degree of anisotropy increases with increasing field strength, so the slope of the polarizations will increase. The polarizations of data points taken at the same laser frequency but at different field strengths will in general not be equal. Although these points have in common the scalar magnitude of the velocity component v_l along \hat{k}_{laser} selected out by the laser, these slices are drawn from different velocity distribution functions with different vector properties; the alignment is not solely dependent on this scalar component. Note in particular that if the observed alignment did somehow depend on the magnitude of v_l alone, then it would be possible to observe alignment in the high- or low-velocity tail of a zero-field Doppler profile, contrary to both intuition and ample experimental evidence.

To obtain an approximate m_j distribution picture, the polarization coefficients were corrected and converted into quadrupole alignment parameters (Sec. IV.B.4). A more thorough discussion of the cause of the systematics present in these

measurements is given in Sec. IV.E. Pragmatically, what was done for these measurements is as follows. A set of diagnostic measurements was performed for each probe geometry; a more extensive set was performed for coaxial than for perpendicular probe. One check involved removing the polarizer from the PMT stack and performing 0/90 degree stack rotations, as if polarization coefficients were being measured. Comparison of these “polarizations” with true polarization measurements taken by locking the PMT stack to one position and manually rotating just the polarizer indicates that the rotation of the entire PMT stack introduces a small degree of variation, which is believed due to small geometrical modulations of the effective detector solid angle as the PMT stack rotations are performed. Coaxial “polarization” measurements taken under plasma conditions at line center with no polarizer in the stack yield a coefficient $\times 100\%$ of -1.59 ± 0.07 . From each pair of these 0/90 degree isotropic measurements, a geometrical correction factor f can be calculated

$$f = \frac{I_{0^0 \text{ measured isotropic}}}{I_{90^0 \text{ measured isotropic}}} = 0.969 \pm 0.004, \quad (4.22)$$

which can then be used to multiplicatively correct the 90 degree background and laser-power corrected LIF intensities for the actual polarization measurements as

$$P(90^0)_{f\text{-corrected}} = \frac{I_{0^0 \text{ measured}} - f I_{90^0 \text{ measured}}}{I_{0^0 \text{ measured}} + f I_{90^0 \text{ measured}}}. \quad (4.23)$$

However, there was an additional unidentified source of spurious polarization in this first experiment. Coaxial laser probe plasma measurements made with the rotation stage locked at 0 degrees and with just the polarizer itself manually rotated to 0/90 degrees yield a polarization coefficient $\times 100\%$ of -1.98 ± 0.07 , indicating that

the geometrical modulation is not the only systematic present. Although not a completely satisfactory treatment, this offset was merely subtracted from the polarizations corrected via Eq. (4.23) to obtain a set of corrected polarizations, as shown in Fig. 4.5. These polarizations and the resultant alignment parameters have been previously tabulated²⁷ and will not be repeated here. Although not satisfactory, this correction scheme does not qualitatively alter the trends shown in the data of Fig. 4.5. Obtaining a more consistent method of correcting for systematics in the polarization measurements was one of the primary motivations for building the stepper-motor-driven PMT stack discussed in Sec. II.D.2

These corrected polarizations can be converted into $A_0^{(2)}$ alignment parameters using the relations in Sec. IV.B.4. The highest polarization observed—+7.5% in the high-velocity tail of the 16 Td data—corresponds to an $A_0^{(2)}$ of -0.15. An approximate m_J distribution picture for the various sub-Doppler “slices” can then be obtained from these alignment parameters and Eq. (4.11) above. The m_J distributions for the 16 Td coaxial data are shown in Fig. 4.6.

2. Rotational quantum state dependence of alignment

All the data in the above section were acquired on a single rotational state. However, there is considerable interest in examining whether different rotational states will exhibit significantly different alignments. The focus of the experiment discussed in this section was on exploring possible relative differences between sub-Doppler polarizations acquired on different rotational lines, taken under otherwise identical conditions. As in Sec. III.D.1, measurements were confined to a single field

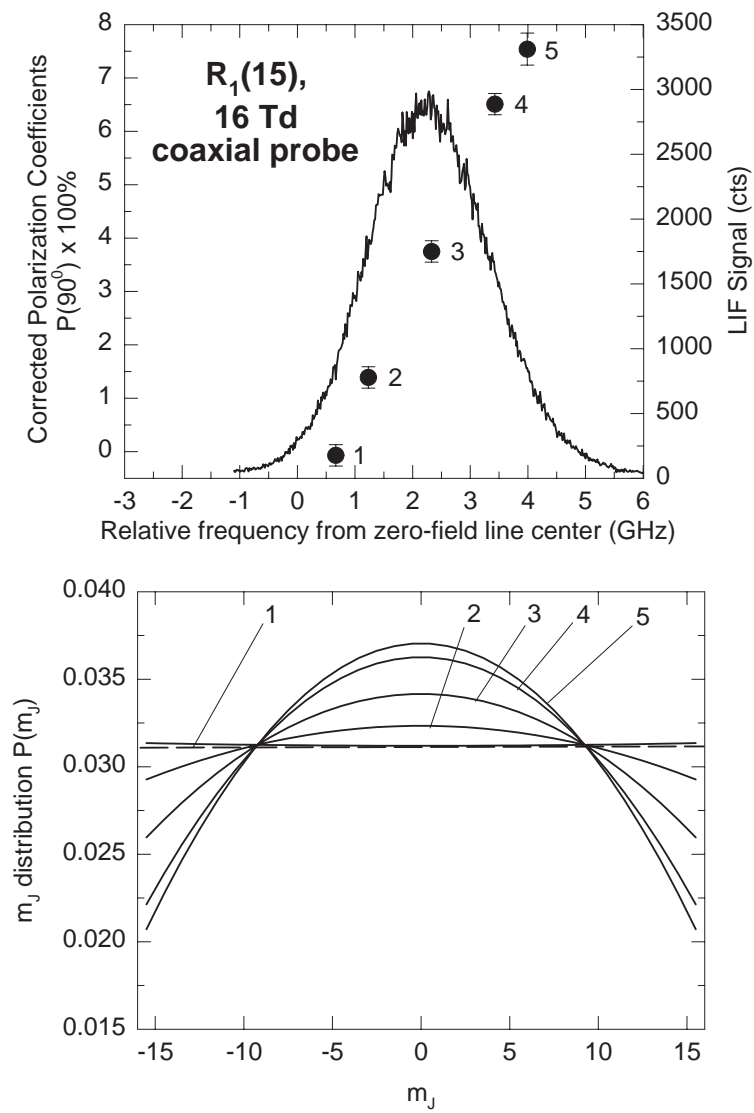


Fig. 4.6: Corresponding m_j distributions derived from the $R_1(15)$ 16 Td coaxial-probe corrected polarization coefficients, as numbered in the top panel.

strength—12 Td—and the parallel probe direction. The stepper-motor driven rotation stage (Sec. II.D.2) and the production conditions of Fig. 2.4 were used throughout. Additionally, observations on the $R_1(15)$ line made under these same conditions with the new stack reconfirm all the trends in the data of the previous section.

Figure 4.7 displays the “raw” data from this set of experiments. Coaxial probe linear polarization coefficients were measured for a total of five rotational lines (four para lines, one ortho) for a variety of laser detunings, all at a fixed field strength of 12.0 Td. The $R_1(N'' = 17)$ transition is not accessible by any combination of ring dye laser birefringent filter/thin etalon/intracavity Brewster plate tunings and thus could not be measured. Additionally, the poor signal-to-background levels of the $R_1(19)$ transition prohibited acquisition of sub-Doppler polarization data on the wings of the transition; the $R_1(20)$ line in the ortho manifold was “substituted” for $R_1(19)$ in order to acquire high-J wing data. The decrease in spacing between the spin-rotation doublets with decreasing N'' prevented acquisition of lower J-state data because the low-velocity tail of the J_1 branch will overlap the high-velocity tail of the J_2 branch, leading to ambiguities in data interpretation. The uncorrected (i.e., background and laser-power-corrected only) polarizations are shown at the relative detunings from the respective line centers at which they were acquired, as determined from a single Gaussian fit to the unpolarized PMT calibration scan. The “hardware marker” method was used to position the ring laser in frequency; the uncertainty in frequency positioning is well-represented by the size of symbols in the figure. The stepper motor driven rotation stage was used exclusively for this experiment. All of these data were

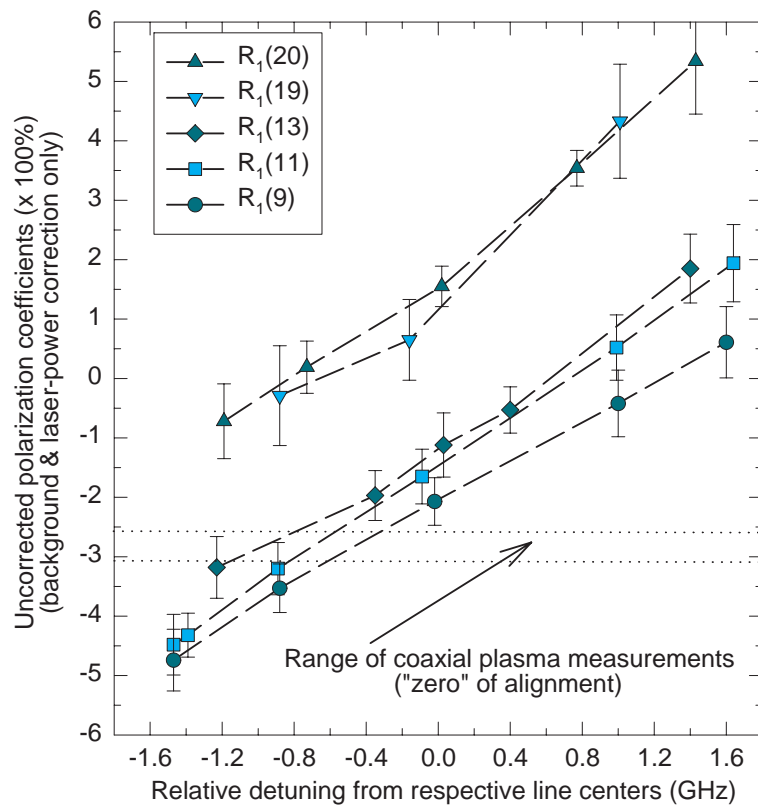


Fig. 4.7: Raw polarization data from rotational state alignment experiment. The sub-Doppler polarizations are shown at the detunings at which they were acquired, relative to the line center of the respective transition. The "hardware marker" method was used to position the laser in frequency space; thus the frequency uncertainty is well-represented by the size of the symbols on the plot. The range of the means of the coaxial probe plasma measurements, shown in Fig. 4.8 (a), is indicated by the dotted lines; these lines are taken as the empirically-determined "line of isotropy" for this experiment.

taken under completely identical laser polarization and fluorescence detection optics. Several of the points in Fig. 4.7 on a given rotational line were acquired on different days, providing excellent corroborating evidence of the reproducibility of the data set.

Because of the unresolved systematics, a very pragmatic approach was taken to determine the “zero” of alignment for each transition. A plasma (all fields off) measurement was made for each of the rotational states at line center to determine what uncorrected polarization corresponds to no alignment. These “raw” polarizations are presented in Fig. 4.8 a). Note that the uncorrected plasma polarizations are reasonably independent of J-state, within error bars, as one would anticipate if the systematic is primarily due to geometrical imaging, as discussed below. Shown in Fig. 4.8 b) are the results of a vertical-matching diagnostic experiment, performed to assess the matching of the laser polarization axis “vertical” with the fluorescence detection axis. This experiment was performed on the $R_1(15)$ transition at line center, in plasma conditions, with coaxial laser probe. The Glan setting of 86 degrees was the minimum of these polarizations; all data shown here were taken with this setting.

The range of plasma polarizations for all rotational lines measured (Fig. 4.8a) is shown by the dotted lines in Fig. 4.7. Note that the “slope” of the polarizations for each rotational line in the figure appears to be essentially the same for all measured rotor states. However, there is a dramatic difference in the “offset” of these lines that is well outside the measurement error bars. The lines shift downward with decreasing J such that for $J = 9.5$ and 11.5 , the low-velocity tail polarizations are considerably below the empirically-determined “line of isotropy”. If the interpretation of these data

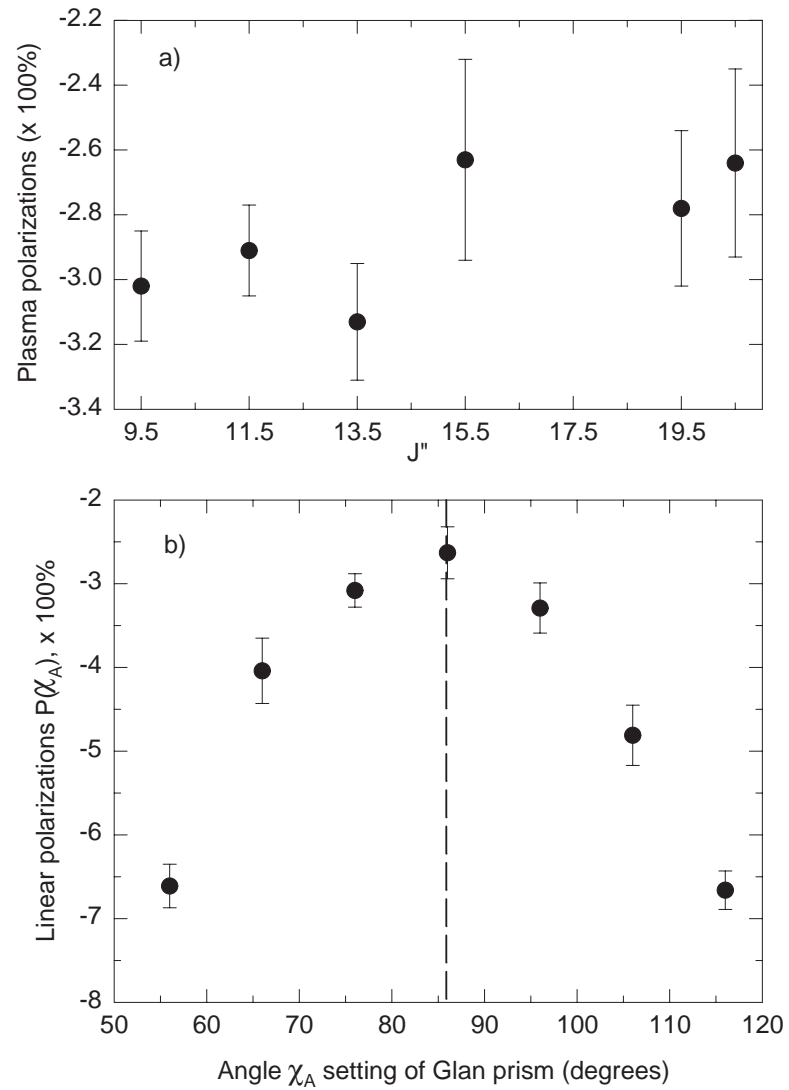


Fig. 4.8: Systematic plasma polarization checks. a) coaxial plasma polarization coefficients as a function of rotational state, measured at line center
 b) χ_A vertical-matching check, performed on $R_1(15)$ at line center.

is correct, the alignment parameter $A_0^{(2)}$ is changing sign from positive (i.e., m_J distribution bowed up) in the low-velocity tail to significantly negative (m_J distribution bowed down) in the high-velocity tail. As discussed in more depth below, we believe that the slopes of the polarizations are related to the change in the relative velocity vector distribution across the Doppler profile. The polarization slopes are the same because all of these states have virtually identical relative vector distributions at 12 Td. The offset of the lines is related to tensor cross section information. These offsets are pronounced because this experiment essentially measures partially-integrated differential cross sections due to the partial velocity selection obtained by measuring polarizations as a function of one component of the ion laboratory velocity. Although not entirely satisfactory, we make the simplest data correction possible to the polarizations by just subtracting off the average plasma polarization for each respective rotational line. These corrected polarizations are shown in Fig. 4.9, along with an additional x-axis that gives the approximate value of the laser-selected velocity component along the tube axis, relative to the mean buffer gas velocity. Both the uncorrected and corrected polarizations are summarized in Table 4.4. The error bars in Figs. 4.7 & 4.9 represent the sample standard deviations of all observations at that particular detuning. Calculations show that these error bars are at or slightly above the Poisson statistics limit, indicating that no other random errors are present.

E. Possible systematics

For any collision-induced alignment experiment, it is essential to have a set of conditions that are known to produce no alignment. These conditions essentially

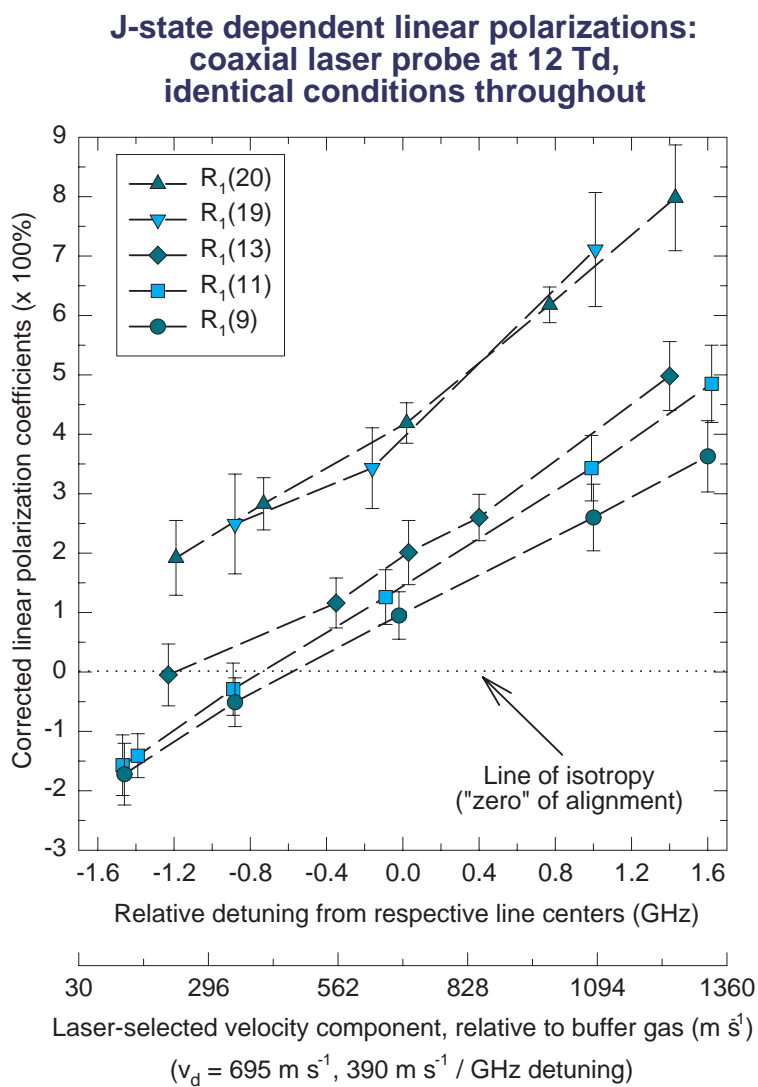


Fig. 4.9: Polarizations of Fig. 4.7, with simple subtractive correction made to each point.

Transition Probed	J''	Detuning (GHz)	# of obs.	Uncorrected $P(90^0) \times 100\%$	Corrected $P(90^0) \times 100\%$
$R_1(9)$	9.5	-1.47	24	-4.74 ± 0.52	-1.72 ± 0.52
$R_1(9)$	9.5	-0.88	24	-3.53 ± 0.41	-0.51 ± 0.41
$R_1(9)$	9.5	-0.02	24	-2.07 ± 0.40	$+0.95 \pm 0.40$
$R_1(9)$	9.5	+1.00	24	-0.42 ± 0.56	$+2.60 \pm 0.56$
$R_1(9)$	9.5	+1.60	24	$+0.61 \pm 0.60$	$+3.63 \pm 0.60$
$R_1(11)$	11.5	-1.47	24	-4.48 ± 0.51	-1.57 ± 0.51
$R_1(11)$	11.5	-1.39	12	-4.32 ± 0.37	-1.41 ± 0.37
$R_1(11)$	11.5	-0.89	24	-3.20 ± 0.44	-0.29 ± 0.44
$R_1(11)$	11.5	-0.09	24	-1.65 ± 0.46	$+1.26 \pm 0.46$
$R_1(11)$	11.5	+0.99	24	$+0.52 \pm 0.55$	$+3.43 \pm 0.55$
$R_1(11)$	11.5	+1.64	24	$+1.94 \pm 0.65$	$+4.85 \pm 0.65$
$R_1(13)$	13.5	-1.23	22	-3.18 ± 0.52	-0.05 ± 0.52
$R_1(13)$	13.5	-0.35	16	-1.97 ± 0.42	$+1.16 \pm 0.42$
$R_1(13)$	13.5	+0.03	16	-1.12 ± 0.54	$+2.01 \pm 0.54$
$R_1(13)$	13.5	+0.40	14	-0.53 ± 0.39	$+2.60 \pm 0.39$
$R_1(13)$	13.5	+1.40	24	$+1.85 \pm 0.58$	$+4.98 \pm 0.58$
$R_1(19)$	19.5	-0.88	24	-0.29 ± 0.84	$+2.49 \pm 0.84$
$R_1(19)$	19.5	-0.16	24	$+0.65 \pm 0.68$	$+3.43 \pm 0.68$
$R_1(19)$	19.5	+1.01	24	$+4.33 \pm 0.96$	$+7.11 \pm 0.96$
$R_1(20)$	20.5	-1.19	24	-0.72 ± 0.63	$+1.92 \pm 0.63$
$R_1(20)$	20.5	-0.73	16	$+0.19 \pm 0.44$	$+2.83 \pm 0.44$
$R_1(20)$	20.5	+0.02	16	$+1.55 \pm 0.34$	$+4.19 \pm 0.34$
$R_1(20)$	20.5	+0.77	16	$+3.54 \pm 0.30$	$+6.18 \pm 0.30$
$R_1(20)$	20.5	+1.43	24	$+5.34 \pm 0.89$	$+7.98 \pm 0.89$

Table 4.4: Polarization data from rotational state alignment experiment. All data was acquired at 12 Td with the coaxial laser probe geometry, with identical polarization optics throughout. The stated detunings are from the respective line centers of the transitions. Error bars represent the sample standard deviation of all polarizations at that particular detuning. The error bars have not been divided by the square root of the number of observations and thus are not standard deviations of the mean.

define the “zero” of alignment and allow one to detect and (hopefully) correct for any systematics present. A very important systematic check for this particular experiment for either probe geometry is performed by recording sub-Doppler polarization measurements with both the charge-separation and drift fields off. As discussed in Chapt. III, the N_2^+ molecules in the resulting plasma experience no field and therefore their velocity distribution should be strictly Maxwell-Boltzmann, with a resulting linewidth characterized by the temperature of the buffer gas. The relative velocity vectors \mathbf{g} of the N_2^+ -He pair are isotropically distributed and no alignment is possible. In principle then, all zero-field $P(90^0)$'s for either probe geometry and at any laser frequency should vanish. Unfortunately, these measurements are not entirely free of spurious polarization, which results in non-zero fluorescence polarization coefficients even in the complete absence of molecular alignment. For this experiment, spurious polarization acts as the major systematic error that affects the accuracy of the alignment parameters calculated from the measured polarization coefficients.

In this experiment, exhaustive checks were performed to determine the cause of this systematic. Frequently-cited causes of spurious polarization, such as stress-induced birefringence on the laser entrance windows or LIF windows, or glancing-angle polarizing reflections off of metallic surfaces were ruled out. One trend noted quite early was that the coaxial laser probe polarizations at plasma line center tend always to be negative, while perpendicular laser probe polarizations tend to be positive. This trend became extremely pronounced once the stepper motor-driven rotation stage was employed. It is now believed that the non-zero polarizations are

primarily geometrical in nature. What is being imaged in this experiment is a bar of fluorescence over a finite, irregularly-shaped solid angle. Changing the probe direction changes the orientation of the bar, thus changing the sign but not the magnitude of the observed polarization. An attempt was made to model this supposition by starting with the generalized expressions for polarization tensor elements.²¹ These elements are functions of two sets of Euler angles. By treating a point fluorescence source and integrating over the set of angles corresponding to variations either along or perpendicular to the tube axis, qualitative correspondence was obtained with the trends observed in the experiment. However, the range of solid angle needed to obtain quantitative correspondence is considerably greater than any of the effective apertures employed. Future work is planned on modeling this problem more comprehensively.

F. Discussion & dynamics theory

Collision-induced rotational alignment is produced by the coupling of anisotropies in both the ion-neutral interaction potential and the relative velocity vector distribution. The contribution of the interaction potential anisotropy can be quantified by the tensor or alignment cross sections $\sigma_{j_i \rightarrow j_f}^{K_i K_f}(g)$, as discussed further below. The contribution of the relative velocity vector anisotropy can be quantified by knowing the velocity distribution function $F(\mathbf{v})$. In general, these two anisotropies are coupled in such a way that disentangling them in an experiment can be difficult. However, because this particular experiment incorporates partial velocity selection, some degree of decoupling of these two anisotropies is possible.

The general morphology of the polarizations (or equivalently, the quadrupole alignment parameters) in Figs. 4.5 and 4.7 can be discussed in terms of the “slopes” and “offsets” of the lines on which the polarization coefficients for a particular rotor state, field strength, and probe direction fall. It is believed that the “slopes” of the polarization lines are related to the degree of anisotropy of the relative velocity vector distributions. The reason for the different slopes in Fig. 4.5 (b) has been discussed above. The slopes in Fig. 4.7 appear independent of quantum state because, at 12 Td, the velocity distribution functions for all of these rotational states are essentially the same. The differences in mobility between rotor states discussed in Sec. III.D.1 are believed to be too small to manifest themselves, within the error bars of the polarization coefficients. Actually, there is some evidence in the data that the slope of the higher J-state lines is slightly greater than the low-J states (compare $R_1(20)$ and $R_1(13)$). It is believed that the “offsets” or absolute value of the polarizations contain tensor cross section information. The dramatic difference between the offsets of the lines in Fig. 4.7 is due to significantly different tensor cross sections for each of the rotational states. These differences are more pronounced than they would be in a fully-velocity averaged experiment because this experiment is measuring partially-integrated differential cross sections, due to the partial velocity selection imposed by the single-frequency laser.

State-to-state or tensor cross sections can be classified as elastic (J-preserving) or inelastic. In general, collision-induced rotational alignment can involve a complex interplay between elastic and inelastic processes. However, for this experiment, the elastic scattering cross sections are predominantly observed. This is because, for the

relatively high-J states studied here, the energy gaps between adjacent rotor states are sufficiently large such that elastic scattering is favored in a scattering event. Furthermore, the use of a single-frequency laser means that the probed section of velocity space is quite small. Thus the probability, in a *single* scattering event, of an individual molecule transferring the necessary energy T->R to scatter inelastically into the interrogated velocity slice, absorb a photon, fluoresce, and make a contribution to the polarization signal is quite low. Loosely, the slice of phase space “real estate” probed by the laser is too small to observe inelastic collisions directly. The majority of the molecules in the chosen slice have been “sloshing” around the particular rotor state for some time, undergoing elastic collisions as they make their way to the slice. Detailed balance implies the converse must be true: the majority of the molecules exiting the chosen slice do so by undergoing elastic collisions. The current speculation for this particular system is that elastic collisions are doing most of the “work” of aligning molecules in velocity subgroups. A given molecule undergoes an inelastic collision into, say, a middle velocity. It can then either “walk” its way through a series of elastic, alignment-creating collisions into a high-velocity subgroup, or through a series of alignment-destroying collisions, to lower-velocities.

The data of Fig. 4.7 can be qualitatively explained by the basic model of Gorter, along with the concept of gyroscopic stability. Molecules with $\mathbf{J} \parallel Z_{lab}$ (“pinwheels”) have larger hard-sphere collisional cross-sections and are more likely to undergo more collisions that move them to slower velocity subgroups. Molecules with $\mathbf{J} \perp Z_{lab}$ (“frisbees”) have smaller cross-sections and have undergone fewer collisions, thus evolving to higher velocity subgroups. Molecules in a higher J-state

are more gyroscopically stable; a “harder” collision with more torque is necessary for them to undergo inelastic scattering. Thus, alignment in these higher J-states is more easily preserved. The observations of Wodtke on CO alignment in a He jet expansion⁹ appear to contradict this experiment. The data of Fig. 4.7 show “fast frisbees” and “slow pinwheels”, while the CO-He expansion results are the opposite. However, Wodtke points out that the key to reconciling these apparent differences is realizing that the drift-tube experiment is analogous to a “reverse-seeded” jet expansion.⁸ The physical picture presented for the CO experiment is that $\mathbf{J} \parallel \mathbf{v}$ molecules (pinwheels) again have larger collisional cross sections with the carrier gas. However, in the jet expansion, these molecules experience a larger average number of collisions and thus get moved forward in the velocity distribution as they are accelerated more efficiently to the terminal velocity of the carrier gas. Molecules with $\mathbf{J} \perp \mathbf{v}$ (frisbees) have smaller cross sections and thus more velocity slip, ending up in the slower velocity groups. Preliminary classical-trajectory work on O_2 expanded in He appears to support this interpretation.²⁸

1. Steady-state fully-velocity averaged theory

A steady-state set of equations that describes the population of the state multipoles T_j^K has been previously derived, first by Meyer *et al.*¹⁴ and subsequently rederived by Follmeg *et al.*¹² The equations are:

$$\begin{aligned}
& \sum_{j_f K_i \lambda} \left(\lambda + \frac{1}{2}\right) T_{j_f}^{K_i} \int_0^\infty dg g^3 \lambda f_{j_f}^{K_i}(g) \lambda \sigma_{j_f \rightarrow j_i}^{K_i K_f}(g) = \\
& \sum_{j_f K_i \lambda} (-)^{2j_i} \left(\lambda + \frac{1}{2}\right) \sqrt{[K_i][K_f][j_f][\lambda]} \times \\
& \begin{pmatrix} K_i & K_f & \lambda \\ 0 & 0 & 0 \end{pmatrix} \begin{Bmatrix} K_i & K_f & \lambda \\ j_i & j_i & j_i \end{Bmatrix} T_{j_i}^{K_i} \int_0^\infty dg g^3 \lambda f_{j_i}^{K_i}(g) \lambda \sigma_{j_i \rightarrow j_f}^{\lambda 0}(g)
\end{aligned} \tag{4.24}$$

where $[X] = 2X + 1$, $\begin{pmatrix} \cdot & \cdot & \cdot \\ \cdot & \cdot & \cdot \end{pmatrix}$ and $\begin{Bmatrix} \cdot & \cdot & \cdot \\ \cdot & \cdot & \cdot \end{Bmatrix}$ are the Wigner 3-j & 6-j symbols and g is the relative speed of the ion-neutral pair. The quantities $\lambda f_j^K(g)$ and $\lambda \sigma_{j_i \rightarrow j_f}^{K_i K_f}(g)$ are the λ th coefficients in the expansion of the relative velocity vector distribution and tensor cross sections in Legendre moments, respectively, and are discussed in greater detail below. The T_j^K are the state multipoles in which the density matrix ρ_{mm}^j can be expressed in the standard expansion²⁴

$$\rho_{mm}^j = \sum_K (-1)^{j-m} \sqrt{2K+1} \begin{pmatrix} j & j & K \\ m & -m & 0 \end{pmatrix} T_j^K \tag{4.25}$$

The T_j^K 's are related to the experimentally obtainable alignment parameters $A_0^{(K)}$ by rescaling factors, given explicitly below.

In both the work of Meyer and Follmeg, a velocity-dependent form of the density matrix expansion of Eq. (4.25) is used:

$$\rho_{mm}^j(\mathbf{v}) = \sum_K (-1)^{j-m} \sqrt{2K+1} \begin{pmatrix} j & j & K \\ m & -m & 0 \end{pmatrix} f_j^K(\mathbf{v}) T_j^K \tag{4.26}$$

where the velocity form factors $f_j^K(\mathbf{v})$ are supposed to contain all of the velocity dependence of the state multipoles T_j^K . However, in both works it is subsequently assumed that all $K > 0$ velocity form factors are equal to the $K = 0$ term that essentially

describes the ion velocity distribution function (independent of alignment). This function just factors out of the density matrix expansion and the K index becomes ignorable. Equation (4.24) can then be written in slightly revised notation by just dropping the K_i superscript on the f 's as:

$$\begin{aligned} \sum_{j_f K_i \lambda} \left(\lambda + \frac{1}{2}\right) T_{j_f}^{K_i} \int_0^\infty dg g^3 \lambda_{f j_f}(g) \lambda \sigma_{j_f \rightarrow j_i}^{K_i K_f}(g) = \\ \sum_{j_f K_i \lambda} (-)^{2j_i} \left(\lambda + \frac{1}{2}\right) \sqrt{[K_i][K_f][j_f][\lambda]} \times \\ \left(\begin{matrix} K_i & K_f & \lambda \\ 0 & 0 & 0 \end{matrix} \right) \left\{ \begin{matrix} K_i & K_f & \lambda \\ j_i & j_i & j_i \end{matrix} \right\} T_{j_i}^{K_i} \int_0^\infty dg g^3 \lambda_{f j_i}(g) \lambda \sigma_{j_i \rightarrow j_f}^{\lambda 0}(g) \end{aligned} \quad (4.27)$$

As pointed out in both works, this means that the velocity distribution function is assumed to be the same for each rotor state, so the j indices in Eq. (4.27) are redundant as well. These assumptions were made for both experimental and theoretical reasons. Experimentally, there were no good measurements of rotor-state dependent velocity distributions; theoretically, there was no good development on what these K -dependent velocity form factors should be. The apparent removal of velocity dependence from the density matrix expansion seems paradoxical, since as the experiment has evolved, the measurements became explicitly concerned with the dependence or correlation of alignment parameters with one component of velocity, and all this information appears to be gone.

Although not solved explicitly by Meyer¹⁴ and discussed briefly by Follmeg,¹² it should be pointed out that Eq. (4.27) describes a practical, working set of equations that can be solved for the state multipoles of any rotor state, given velocity distribution functions and tensor cross sections for each rotor state, the two

ingredients that are the real physical content of these equations. The structure of these equations is discussed in more detail in the thesis of Follmeg.²⁹ Equation (4.27) can be written in matrix form as:

$$\mathbf{A} \vec{T} = \mathbf{B} \vec{T} \quad \text{with solution} \quad \mathbf{B}^{-1} \mathbf{A} \vec{T} = \vec{T} \quad (4.28)$$

where matrix \mathbf{A} is associated with the right hand (“depopulation”) side of Eq. (4.27), and \mathbf{B} with the left hand (“population”) side. It should be pointed out that the key to understanding the matrix structure of this equation is recognizing that j_i and K_f are free indices, i.e., Eq. (4.27) must be true for any choice of j_i and K_f . There is an analogy to a much simpler set of kinetic or master equations that describe just the populations of each state, which allows the structure of \mathbf{A} and \mathbf{B} to be easily seen. As discussed by Follmeg, Eq. (4.28) can then be solved for the solution vector \vec{T} as an eigenvector equation. The solution vector \vec{T} is the eigenvector of matrix $\mathbf{B}^{-1} \mathbf{A}$ associated with the eigenvalue 1 and can be found numerically. The elements T_j^K of the solution vector can then be related to the experimentally-obtainable alignment parameters $A_0^{(K)}$ through the relation:

$$T_j^K = \frac{\sqrt{2K+1}}{\langle j \| J^{(K)} \| j \rangle} \langle J_0^{(K)} \rangle \quad (4.29)$$

where the $\langle J_0^{(K)} \rangle$ are ensemble averages of the spherical tensor operators.³⁰

Explicitly, for the $K=2$ and 4 quadrupole and hexadecapole alignment parameters, the relations are:

$$A_0^{(2)} = \frac{\sqrt{6}}{j(j+1)} \frac{\langle j \| J^{(2)} \| j \rangle}{\sqrt{5}} T_j^2 \quad A_0^{(4)} = \frac{\sqrt{70}}{4j^2(j+1)^2} \frac{\langle j \| J^{(4)} \| j \rangle}{\sqrt{9}} T_j^4 \quad (4.30)$$

with the reduced matrix elements given by Eq. (4.10) above. As discussed by Follmeg,¹² to match up a numerically-calculated \vec{T} vector with experimentally-obtained alignment parameters via Eq. (4.27), the \vec{T} vector must be normalized such that the trace of each j th sub-block of the density matrix equals 1, i.e., the T_j^K 's must satisfy:

$$\sum_m \rho_{mm}^j = \sum_m \sum_K (-1)^{j-m} \sqrt{2K+1} \begin{pmatrix} j & j & K \\ m & -m & 0 \end{pmatrix} T_j^K = 1 \quad (4.31)$$

The tensor cross sections $\lambda \sigma_{j_i \rightarrow j_f}^{K_i K_f}(g)$ introduced above must be obtained from a close-coupled scattering calculation. These λ -labeled cross sections can be explicitly related to transition (T) matrix elements that are produced in the scattering calculation, albeit through a non-trivial angular momentum recoupling sum. Previously, Follmeg *et al.*¹² obtained these cross sections by modifying the Hibridon suite of code³¹ to calculate the λ -labeled tensor cross sections. An attempt was made to rerun the Hibridon code for higher- J states, but this calculation could not be completed because of time considerations. It should be noted that Hibridon calculates scalar cross sections that have been decomposed into Legendre moments. In principle then, the vector tensor cross section could be unambiguously reconstructed just from the existing Hibridon code. These tensor cross sections can be related to the more familiar state-to-state cross sections by a recoupling transformation. Explicitly, the relations are:

$$\begin{aligned}
\sigma_{j_i \rightarrow j_f}^{K_i K_f}(\mathbf{g}) &= \sum_{\lambda} \lambda \sigma_{j_i \rightarrow j_f}^{K_i K_f}(\mathbf{g}) P_{\lambda}(\cos \theta) \quad \text{and} \\
\sigma_{j_i m_i \rightarrow j_f m_f}(\mathbf{g}) &= \sum_{K_i} \sum_{K_f} (-1)^{j_i + j_f - m_i - m_f} \sqrt{2K_i + 1} \begin{pmatrix} j_i & j_i & K_i \\ m_i & -m_i & 0 \end{pmatrix} \times \\
&\quad \sqrt{2K_f + 1} \begin{pmatrix} j_f & j_f & K_f \\ m_f & -m_f & 0 \end{pmatrix} \sigma_{j_i \rightarrow j_f}^{K_i K_f}(\mathbf{g})
\end{aligned} \tag{4.32}$$

Although the state-to-state picture is more familiar and intuitive, experimentally it is often too detailed or “fussy”. Usually, one can only get a broad or blurry picture of the underlying microscopic cross-sections, and so the tensor cross section picture is usually more appropriate for collision-induced alignment experiments.

2. Partial velocity selection

Unfortunately, the formalism developed for the original broadband experiment is not appropriate for this experiment, in which one laboratory component of ion velocity is essentially completely specified by the single-frequency LIF technique. Equation (4.24) above was derived starting from a statement of detailed balance at steady-state for each rotor state $|j_i m_i\rangle$:

$$\sum_{j_f=0}^{\infty} \sum_{m_f=-j_f}^{j_f} k_{j_f m_f \rightarrow j_i m_i} \left[|j_f m_f\rangle \right] = \sum_{j_f} \sum_{m_f} k_{j_i m_i \rightarrow j_f m_f} \left[|j_i m_i\rangle \right] \tag{4.33}$$

where the k 's are fully-velocity averaged state-to-state rate constants:

$$k_{j_i m_i \rightarrow j_f m_f} = \int_{-\infty}^{+\infty} d^3 v_1 \int_{-\infty}^{+\infty} d^3 v_2 f_1(\mathbf{v}_1) \rho_{m_i m_i}^{j_i}(\mathbf{v}_2) |\mathbf{g}| \sigma_{j_i m_i \rightarrow j_f m_f}(\mathbf{g}) \tag{4.34}$$

The buffer gas coordinates in Eq. (4.34) are denoted with “1” subscripts, and the ion molecule coordinates are denoted with “2” subscripts. Note that Eq. (4.34) already contains *integral* state-to-state cross sections. For the case here, it is necessary to start

with a detailed balance equation that involves differential cross sections, and attempt to integrate these over center-of-mass coordinates to obtain integral cross sections.

The starting equations might be:³²

$$\begin{aligned} & \sum_{j_f} \sum_{m_f} \int_{-\infty}^{+\infty} d^3 \mathbf{v}_1 \int_{-\infty}^{+\infty} d^2 \hat{\mathbf{v}}_{2f} d^3 \mathbf{v}_{2i} f_1(\mathbf{v}_1) \rho_{m_i m_i}^{j_i}(\mathbf{v}_{2i}) |\mathbf{v}_{2i} - \mathbf{v}_1| \frac{d\sigma}{d\Omega}_{j_i m_i \rightarrow j_f m_f}(\mathbf{g}_i, \theta_{if}) \\ &= \sum_{j_f} \sum_{m_f} \int_{-\infty}^{+\infty} d^3 \mathbf{v}_1 \int_{-\infty}^{+\infty} d^3 \mathbf{v}_{2f} f_1(\mathbf{v}_1) \rho_{m_f m_f}^{j_f}(\mathbf{v}_{2f}) |\mathbf{v}_{2f} - \mathbf{v}_1| \frac{d\sigma}{d\Omega}_{j_f m_f \rightarrow j_i m_i}(\mathbf{g}_f, \theta_{if}) \end{aligned} \quad (4.35)$$

with $\mathbf{g}_i = \mathbf{v}_{2i} - \mathbf{v}_1$, $\mathbf{g}_f = \mathbf{v}_{2f} - \mathbf{v}_1$ and θ_{if} the angle between \mathbf{v}_{2i} and \mathbf{v}_{2f} . This set of equations is completely analogous to the starting point of the fully-velocity averaged equations, except that another index has been added, the velocity vector \mathbf{v}_{2i} . The left and right-hand sides of Eq. (4.35) describe the depopulation and population of the lab velocity-labeled rotor state $|j_i m_i\rangle(\mathbf{v}_{2i})$. On the left hand side, the integrands can be rearranged to obtain an integral cross section fairly easily as:

$$\int d^2 \hat{\mathbf{v}}_{2f} \frac{d\sigma}{d\Omega}_{j_i m_i \rightarrow j_f m_f} = \sigma_{j_i m_i \rightarrow j_f m_f}(\mathbf{g}_i) \quad (4.36)$$

(the ‘‘hat’’ notation denotes an angular integral). In words, this is because we are just concerned with the depopulation of a particular chosen vector \mathbf{v}_{2i} into all possible final vectors. However, the right hand side, problems are encountered as the center-of-mass velocity \mathbf{G} cannot be easily integrated out of the population differential cross section. This is because, loosely, one needs to integrate over all final lab velocity vectors \mathbf{v}_{2f} in a ‘‘funny way’’ to get the particular \mathbf{v}_{2i} chosen. This complication makes it much harder to ‘‘integrate out’’ to an integral cross section that could in principle be calculated by some formalism. This is because the differential cross

sections that depend on relative velocity must be integrated in such a way as to meet the “constraint” imposed by completely specifying one vector component in the lab frame. Additionally, because this is not a single-collision experiment, there is no concept of “before” and “after” or initial and final. All that can be known is that the molecules observed were in a particular quantum state and have one completely specified component of velocity.

A heuristic that was developed early on in this experiment was to argue that the introduction of an idealized single-frequency probe laser cannot change any of the angular momentum recoupling terms or any of the sums or indices in Eq. (4.27). If it is assumed that only the integrals in this equation can change, we can make an *ansatz* that the degree of partial velocity selection imposed by the probe laser means that the quadrupole alignment observed in this experiment depends on integrals of the form

$$A_0^{(2)}(v_l, \hat{\mathbf{k}}) \propto I_2 = \int_0^{+\infty} dg \, g^3 F(g; v_l, \hat{\mathbf{k}}) f_{\lambda=2}(g)^{\lambda=2} \sigma(g) \quad (4.37)$$

where the K_i, K_f and j_i, j_f indices on the relative velocity vector distribution and tensor cross sections have been suppressed. $F(g; v_l, \hat{\mathbf{k}})$ is a “narrowing” function introduced into these integrals by probing in a specific direction $\hat{\mathbf{k}}$ with respect to the Z-axis with a tunable single-frequency laser that picks out a specific laboratory velocity component v_l of the molecule along $\hat{\mathbf{k}}$. The physical interpretation of $F(g; v_l, \hat{\mathbf{k}})$ is that it is the relative speed distribution of the “slice” of molecular laboratory velocities selected out by the laser probing in a specific direction at a specific detuning. For probing parallel to Z_{lab} , $F(g; v_l, \hat{\mathbf{k}} = 0^0) dg$ is the probability,

parameterized by laser-selected molecule lab component $v_z = v_l$, of measuring a relative speed of a colliding ion-buffer pair between g and $g + dg$. One can work out an explicit form for $F(g; v_l, \hat{\mathbf{k}})$ for this probe direction, borrowing some math from experiments of Prichard *et al.* on inelastic collision cross sections on excited-state alkali dimers³³

$$F(g; v_l, \hat{\mathbf{k}} = 0^0) dg = \frac{g}{2\sqrt{r+1} s_p^2} \exp\left[\frac{-(g^2 - (r+1) v_l^2)}{2(r+1) s_p^2}\right] \left\{ \operatorname{erf}\left(\frac{g + (r+1) v_l}{\sqrt{2r(r+1)} s_p}\right) + \operatorname{erf}\left(\frac{g - (r+1) v_l}{\sqrt{2r(r+1)} s_p}\right) \right\} dg \quad (4.38)$$

with $r = \frac{m_2 T}{m_1 T_\perp}$ and $s_p = \sqrt{\frac{k_B T_\perp}{m_2}}$

The $\lambda=2$ indices in Eq. (4.37) come from an “index-matching” heuristic. The key cross section is the ${}^\lambda \sigma_{j_f \rightarrow j_i}^{K_i K_f} = {}^2 \sigma_{j_f \rightarrow j_i}^{02}$ term on the population (left-hand) side of Eq. (4.x), which is the anisotropic piece of this tensor cross section associated with the $\lambda=2$ piece of the relative velocity vector distribution.³⁴ This term essentially describes the transfer of population from the unaligned ensemble ($K_i = 0$, “ $P_0(\cos\theta)$ ” character) to quadrupole alignment ($K_f = 2$, “ $P_2(\cos\theta)$ ” character) for a particular j_i . Its counterpart on the depopulation (right hand) side of Eq. (4), is the ${}^\lambda \sigma_{j_i \rightarrow j_f}^{\lambda_i 0} = {}^2 \sigma_{j_i \rightarrow j_f}^{20}$ term, which transfers population out of the $K_i = 2$ multipole in some j_i state to the unaligned $K_f = 0$ multipoles in various other rotor states.

The integral I_2 in Eq. (4.37) can be calculated for various experimentally-representative values of the relative velocity vector distribution, and various laser

detunings. If a three-temperature ion velocity distribution of the form of Eq. (3.23) is used, with a buffer gas velocity distribution given by Eq. (3.29), then the ion-buffer relative velocity vector distribution can be derived analytically.¹⁴ The $\lambda=2$ moments of this relative velocity vector distribution can then be calculated numerically. The I_2 integral will formally mimic the sub-Doppler parallel probe experimental data for almost any form of tensor cross section in the integral. Although this calculation is extremely simplistic, there are some additional arguments one can give that make it more appealing. Since it is assumed that the probe laser cannot modify the full velocity vector distribution or the collision dynamics, the probe observation function $F(g; v_l, \hat{\mathbf{k}})$ would be expected to appear as a product with moments of both the full distribution and the tensor cross sections. Also, $F(g; v_l, \hat{\mathbf{k}})$ needs to multiply some moment of the *full* relative velocity vector distribution because, from the experimental data, it is clear that sub-Doppler alignment does not depend on the magnitude of v_l alone. What primarily distinguishes two different “slices” from two Doppler profiles at different field strengths but at the same laser detuning v_l is the vector properties of the *entire* distribution from which they are drawn. Additionally, this heuristic model correctly predicts no alignment for the isotropic (zero-field) case, since then all $\lambda>0$ Legendre moments of the relative velocity vector distribution vanish and thus integrals of the form of Eq. (4.37) vanish as well. Unfortunately, this *ansatz* is just that—an educated guess at the form of the answer, and has not be incorporated into either the fully or partially-velocity selected formalism discussed above. An appropriate theory developed from first principles has not appeared at this writing.

G. Conclusions

It has been demonstrated that LIF rotational alignment experiments involving charged species in a drift tube or plasma environment are possible. A fairly powerful methodology for measuring alignment parameters by single-frequency polarized LIF has been detailed. For N_2^+ drifted in He, a strong correlation is found between the degree of rotational alignment for a single rotational line and the velocity subgroup when probed parallel to the tube axis. Furthermore, a dramatic difference in velocity-selected alignment as a function of rotational state is observed when probing coaxially for a fixed field strength (12 Td). The slopes of these polarization curves are believed related to the relative velocity distribution of the ion-buffer pair; the offsets of the curves are believed to be giving tensor cross section information about the probed states. Additionally, it appears that, for sufficiently low rotational state, the quadrupole alignment parameter is changing sign across the Doppler profile, behavior that has not been observed in a collision-induced rotational alignment experiment before, to the best of this investigator's knowledge. There is evidence presented here that supports the hypothesis that velocity-subgroup alignment is the "generic" behavior of any gas phase system in which there is some sort of anisotropic (non-Maxwell-Boltzmann) velocity distribution.

References for Chapter IV

1. M. P. Sinha, C. D. Caldwell, and R. N. Zare, *J. Chem. Phys.* **61**, 491 (1974).
2. D. P. Pullman, B. Friedrich, and D. R. Herschbach, *J. Chem. Phys.* **93**, 3224 (1990).
3. B. Friedrich, D. P. Pullman, and D. R. Herschbach, *J. Phys. Chem.* **95**, 8118 (1991).
4. M. J. Weida and D. J. Nesbitt, *J. Chem. Phys.* **100**, 6372 (1994).
5. V. Aquilanti, D. Ascenzi, D. Cappelletti, and F. Pirani, *Nature (London)* **371**, 399 (1994).
6. V. Aquilanti, D. Ascenzi, D. Cappelletti, and F. Pirani, *J. Phys. Chem.* **99**, 13620 (1995).
7. V. Aquilanti, D. Ascenzi, D. Cappelletti, R. Fedeli, and F. Pirani, *J. Phys. Chem. A* **101**, 7648 (1997).
8. 1997 Conference on the Dynamics of Molecular Collisions (Cragun's Conference Center on Gull Lake, Brainerd MN, July 20-25, 1997).
9. S. Harich and A. M. Wodtke, *J. Chem. Phys.* **107**, 5983 (1997).
10. R. A. Dressler, H. Meyer, and S. R. Leone, *J. Chem. Phys.* **87**, 6029 (1987).
11. S. Miller, J. Tennyson, B. Follmeg, P. Rosmus, and H.-J. Werner, *J. Chem. Phys.* **89**, 2178 (1988).
12. B. Follmeg, P. Rosmus, and H.-J. Werner, *J. Chem. Phys.* **93**, 4687 (1990).
13. B. Follmeg, H.-J. Werner, and P. Rosmus, *J. Chem. Phys.* **95**, 979 (1991).
14. H. Meyer and S. R. Leone, *Mol. Phys.* **63**, 705 (1988).
15. H. Meyer and S. R. Leone, *J. Chem. Phys.* **105**, 5858 (1996).
16. M. J. Weida, Ph. D. Thesis, University of Colorado (1996).
17. C. J. Gorter, *Naturwissenschaften* **26**, 140 (1938).
18. W. R. Sanders and J. B. Anderson, *J. Phys. Chem.* **88**, 4479 (1984).

19. e.g., R. N. Zare, *Angular Momentum: Understanding Spatial Aspects in Chemistry and Physics* (Wiley-Interscience, New York, 1988), Chapter 3, Eq. (3.37).
20. H. Meyer (private communication, 1993); E. B. Anthony (private calculation, 1995).
21. C. H. Greene and R. N. Zare, *J. Chem. Phys.* **78**, 6741 (1983).
22. R. N. Zare, *Angular Momentum: Understanding Spatial Aspects in Chemistry and Physics* (Wiley-Interscience, New York, 1988).
23. C. H. Greene and R. N. Zare, *Annu. Rev. Phys. Chem.* **33**, 119 (1982).
24. K. Blum, *Density Matrix, Theory and Applications* (Plenum Press, New York, 1981).
25. A. J. Orr-Ewing and R. N. Zare, *Annu. Rev. Phys. Chem.* **45**, 315 (1994).
26. J. L. Kinsey, *Ann. Rev. Phys. Chem.* **28**, 349 (1977).
27. E. B. Anthony, W. Schade, M. J. Bastian, V. M. Bierbaum, and S. R. Leone, *J. Chem. Phys.* **106**, 5413 (1997).
28. J. Fair, private communication (1998).
29. B. Follmeg, Ph. D. Thesis, Johann Wolfgang Goethe University, Frankfurt am Main, Germany (1990).
30. R. N. Zare, *Angular Momentum: Understanding Spatial Aspects in Chemistry and Physics* (Wiley-Interscience, New York, 1988); Chapter 5, p. 227.
31. D. E. Manolopoulos, *J. Chem. Phys.* **85**, 6425 (1986); M. H. Alexander and D. E. Manolopoulos, *J. Chem. Phys.* **86**, 2044 (1987).
32. H. Meyer, private communication (1997).
33. N. Smith, T. A. Brunner, R. D. Driver, and D. E. Pritchard, *J. Chem. Phys.* **69**, 1498 (1978); N. Smith, T. A. Brunner, and D. E. Pritchard, *J. Chem. Phys.* **74**, 467 (1981); T. P. Scott, N. Smith, and D. E. Pritchard, *J. Chem. Phys.* **80**, 4841 (1984).
34. R. Parson, private communication (1996).